IEEE Access
Multidisciplinary | Rapid Review | Open Access Journal

Received January 1, 2022, accepted January 19, 2022, date of publication January 27, 2022, date of current version February 3, 2022.

Digital Object Identifier 10.1109/ACCESS.2022.3147357

Voltage Restoration Control for Microgrid With Recurrent Wavelet Petri Fuzzy Neural Network

FAA-JENG LIN, (Fellow, IEEE), JEN-CHUNG LIAO, CHENG-I CHEN, (Member, IEEE), PIN-RONG CHEN, AND YU-MING ZHANG

Department of Electrical Engineering, National Central University, Chungli 320, Taiwan

Corresponding author: Faa-Jeng Lin (linfj@ee.ncu.edu.tw)

This work was supported by the Ministry of Science and Technology of Taiwan under Grant MOST 110-3116-F-008-001.

ABSTRACT This study presents a voltage restoration control (VRC) based on battery energy storage system (BESS), which can be used for both supporting power source and voltage compensation. Voltage restoration is an important task for the power control of microgrid during utility disturbances. One of the disturbances is caused by short circuit on power line of the microgrid, which may lead to voltage sag and even blackout of the microgrid system. To tackle this problem, the recurrent wavelet petri fuzzy neural network (RWPFNN) controller is proposed in this study for the VRC of BESS to provide fast control response to mitigate the transient impact. Moreover, to examine the compliance with the requirements of low voltage ride through (LVRT) of the photovoltaic (PV) plant and investigate the performance of the proposed VRC, the microgrid built in Cimei Island in Penghu Archipelago, Taiwan, is investigated. Furthermore, the PV system, the wind turbine generator (WTG) system and the BESS are connected to the same point of common coupling (PCC) with separated step-up transformers in the microgrid. In addition, the diesel generators provide the main power sources and form the isolated microgrid system. Through the hardware in the loop (HIL) mechanism, which is built using OPAL-RT real-time simulator, with two floating-point digital signal processors (DSPs), the effectiveness of proposed intelligent controllers can be verified and demonstrated.

INDEX TERMS Battery energy storage system, low voltage ride through, microgrid, recurrent wavelet petri fuzzy neural network, voltage restoration control.

ABBREVIATIONS TABLE

Abbreviation	Meaning.
RERs	Renewable energy resources.
PV	Photovoltaic plant.
WTG	Wind turbine generator.
BESS	Battery energy storage system.
LVRT	Low voltage ride through.
VRC	Voltage restoration control.
DESs	Distributed energy sources.
STATCOM	Static synchronous compensator.
SDBR	Series dynamic braking resistor.
DGs	Distributed generators.
PI	Proportional-integral.
DVR	Dynamic voltage restorer.
PCC	Point of common coupling.
VPPs	Virtual power plants.
NNs	Neural networks.
FNNs	Fuzzy neural networks.
PN	Petri net.
WFNN	Wavelet fuzzy neural network.
WPFNN	Wavelet petri fuzzy neural network.
RFNN	Recurrent fuzzy neural network.
RWFNN	Recurrent wavelet fuzzy neural network.
RWPFNN	Recurrent wavelet petri fuzzy neural network.
HIL	Hardware in the loop.
DSPs	Digital signal processors.
PWM	Pulse width modulation.
SOGI-PLL	Second-order generalized integrator.
MPPT	Maximum power point tracking.
SPWM	Sinusoidal PWM.
PMSG	Permanent magnet synchronous generator.
BP	Backpropagation.
SPI	Serial peripheral interface.
FPGA	Field Programmable Gate Array.

The associate editor coordinating the review of this manuscript and approving it for publication was Lasantha Meegahapola.

IAE	Integral absolute error.
MAE	Maximum absolute error.
FCL	Fault current limiter.

I. INTRODUCTION

To fight the climate change requires the actions including greenhouse gas emissions reduction, energy efficiency improvement, renewable energy portfolios, and policies aimed at slowing climate change to keep the global warming under 2 degrees Celsius. One of the most effective way is to promote the penetration level of the RERs, such as PV plant, WTG and BESS. Owing to its ability to integrate various kinds of RERs, the microgrid system has gotten increasing attention recently as means toward a greener future all over the world [1], [2]. However, some technical challenges are necessarily taken into consideration, for instance, voltage regulation, reliable operation during short-circuit faults, and reactive power management [3]–[5].

The proposed voltage restoration strategy has two components: one is the regulatory grid code, which is the requirements of LVRT to support grid operations, and the other is the VRC during voltage sags. The LVRT requirements have been applied to WTGs, and recently PVs are also required to fulfill these grid codes [6], [7]. E.ON-Netz, a power company of Germany, is the first to issue LVRT requirements for DESs, in which the DESs have to remain on grid and inject reactive power into the grid during grid faults [8]. Though the published requirements are for the DESs connected to the high-voltage system, these requirements can also be applied to the medium or low-voltage systems. When the voltage drops below the limit curve of the E.ON grid requirements, the DESs must inject additional reactive current into the grid amounting to 2% of the rated current for each 1% of the voltage drop to support grid voltage recovery [9], [10]. Certainly, the injection of reactive current of 100% of the rated current is necessary when the voltage drops below 50% of the nominal voltage. Since the proposed control strategy is developed to control the power of the grid-connected PV system to satisfy the most stringent grid requirements, the E.ON LVRT requirements will be used in this study to determine the ratio of the required reactive current during grid faults.

In terms of voltage restoration during voltage sags, the unbalanced grid voltage sags will worsen the performance of microgrid, especially load tripping and degradation of grid-connected devices. In order to overcome these disadvantages, many advanced techniques have been proposed for minimizing network disturbances during grid faults. A STATCOM combined with a small SDBR was studied in [11] to enhance the stability of a wind farm composed of a fixed-speed WTG system. In recent years, load sharing among DGs for voltage restoration became popular inspired by the idea of cooperative control with DGs in multi-DG microgrid [12]–[14]. In [12], the active and reactive droop control were used to maintain active and reactive power sharing among parallel DGs in the primary control, then PI regulators were used to control reactive power and voltage with the references obtained from the dynamic consensus algorithm. Moreover, some researches have been implemented with DVR in the past decade to mitigate voltage disturbances and sags including three-phase voltage unbalance and short circuit [15]–[18]. To restore the PCC voltage and protect the DVR itself for voltage disturbances, a multifunctional DVR control strategy with current limitation has been proposed in [15]. In [16], an innovative designed DVR has been developed by using the PI controller method in *dq0* coordination to attest the mitigation of power quality disturbance in secondary distribution transformer networks due to voltage variation and voltage unbalance. In [17], the effectiveness of the DVR to mitigate voltage disturbances in a hybrid PV-wind system was demonstrated. Furthermore, an inverter-based DVR topology by using the adaptive noise canceling technique for both voltage compensation and harmonic mitigation was investigated in [18]. In addition, the control of DVR for fast detection and corresponding compensation plays a significant role, and several studies have been done on the relative aspects to improve the performance of DVR. A pseudo-derivative-feedback based voltage controller was implemented in [19] for more effective operation of DVR under voltage disturbances. In [20], the DVR using a PI controller based gradient adaptive-variable step-size least mean square control algorithm was proposed to make the control robust and assure better control performance.

Due to the intermittent nature of solar and wind energy, the grid-connected PV and WTG system with BESS have been in use for many demand-related issues to mitigate the intermittency of renewable energy and to support the reactive power [21], [22]. Moreover, the BESS can maintain seamless operation even for the most severe voltage-sag conditions. Thus, the grid-connected BESS can guarantee high availability and flexibility of a power system [23]. Besides the above benefits of the grid-connected BESS, the novel benefits of the BESS for the microgrid are the peak demand management and voltage sags mitigation by supplying different amounts of active and reactive power for the support of frequency and voltage [24], [25]. Owing to the charging and discharging characteristics of BESS, several works have been done on using the BESS as agents for power management in recent years. The BESS is adopted as battery ancillary services in [26] to provide a good utilization of renewables and maintain the desired DC-link voltage. In [27], a clustering algorithm was applied to cluster batteries with similar power demand and capacity into VPPs in order to reduce the line currents and power losses in the microgrid. From the above literature, it is found that the recent research works are focused on DVR and voltage regulation by utilizing BESS in microgrid, while BESS gets more and more attentions since it has been an essential part in a microgrid. Nevertheless, all the voltage regulator, voltage variance regulator, or reactive power regulator mentioned above adopted PI-based control mechanism for the voltage restoration. However, the control performance of the PI control system will be degraded in the

microgrid owing to the nonlinearities and uncertainties of the controlled plants in the microgrid.

It is well known that a combination of NNs and fuzzy logic possesses the advantages of artificial learning in modeling the system dynamics and the benefits of fuzzy reasoning in handling uncertain information. The combined FNNs have been demonstrated being effective in different control applications [28], [29]. Moreover, the PN has been developed into a powerful and effective tool for the concurrent, distributed, parallel, asynchronous, and uncertain information processing systems owing to its analytical and graphical capabilities [30]. Recently, the WFNN has successfully increased the convergence speed and enhanced the computational preciseness with the time-frequency characteristics of wavelet [31]. Furthermore, the WPFNN control combining the merits of the stability of petri network and the time-frequency characteristics of wavelet was proposed in [32] for wind power applications. In addition, some research studies have successfully combined the recurrent structure with FNN and WFNN, that is, the RFNN and RWFNN, in the applications of various fields [33], [34]. In this study a RWPFNN, in which the outputs of wavelet-petri layer are multiplied by the outputs of the FNN with recurrent structure in the outputs of rule layer, is proposed to improve the control performance of the controlled plants.

The microgrid model of Cimei Island [35]–[37] is devised to emulate the operation of a microgrid system in this study. Two control strategies are designed to fulfill the voltage regulation during grid faults: the control of PV to satisfy the requirements of LVRT support according to the grid codes; the control of BESS to implement VRC while sags happen. In the PV control strategy, the E.ON grid requirements are applied for the injection of reactive current when the voltage drops. Moreover, in the BESS control strategy, the active and reactive power provision schemes are developed to emulate the voltage restoration of a microgird. Furthermore, in order to test the performance of the voltage restoration, two different short-circuit fault conditions are designed. In addition, to improve the control performance of the voltage restoration, a RWPFNN controller is developed. Since the proposed RWPFNN comprises both the WPFNN and recurrent structure, the transient control performance of VRC in a microgird can be much improved. Additionally, this article is the extended study of [37], in which the voltage stabilization control methods are investigated for stabilizing grid transition from the grid-connected mode to the islanded mode. In this study, further research for enhancing the function of microgrid with voltage restoration strategy during grid faults in Cimei Island microgrid is proposed. The major contributions of the proposed voltage restoration strategy using intelligent control are: (1) the reactive power control and VRC of BESS use the same controller and coordinate transformation to reduce the design complexity; (2) the fast voltage restoration during grid faults by using VRC of BESS can provide smooth operation of the microgrid system; (3) the RWPFNN controller is proposed to improve the voltage restoration and active power control performance of BESS; (4) the voltage restoration strategy and the proposed RWPFNN controller are successfully implemented in a DSP-based microgrid power system built with OPAL-RT real-time simulator.

The rest of this study is organized as follows: the control strategies of microgrid for the PV and BESS are presented in Section II. The network structure, online learning algorithm and the convergence analysis of the proposed RWPFNN are derived in Section III. To verify the performance of the proposed controllers, the HIL mechanism, which is built using OPAL-RT real-time simulator OP4510, is developed with two floating-point DSPs the Texas Instruments TMS320F28335 for the LVRT control and VRC, respectively, and some comprehensive case studies in the Cimei Island microgrid are investigated in Section IV. Finally, some conclusions are presented in Section V.

II. CONTROL STRATEGY OF MICROGRID

Cimei Island is situated at the southernmost tip of the Penghu Archipelago, which lies in the Taiwan Strait. To promote the penetration rate of renewable energy and storage system, Taiwan Power Company (Taipower) has implemented an isolated microgrid in Cimei Island [35]–[37]. The single-line diagram of Cimei Island is shown in Fig. 1 including two diesel generators, a 355-kWp PV system, a 1000-kWh BESS and a wind farm with 305-kW WTG system. Moreover, the diesel generators provide the main power sources and form the grid-connected power system. The PV system, BESS and the WTG system are connected to the same PCC with separated step-up transformers on Bus 1. For the promotion of usage for the renewable energy and storage system, only 1 diesel generator is switched-on generally. Since the BESS system would play an important role to support and stabilize the microgrid operation, the control strategy is focused on the voltage restoration for the active and reactive control during faults. On the other hand, the PV system is responsible for the LVRT control to meet the requirements of voltage support.

Figure 2 displays the active and reactive power control structure of PV system. In Fig. 2, P_m^* and P are the active power command and active power; Q_m^* and Q are the reactive power command and reactive power; P_{LVRT}^* and Q_{LVRT}^* are the required active and reactive power command during LVRT; v_a, v_b and v_c are three-phase voltages; i_a, i_b and i_c are three-phase currents; I_d^* and I_q^* are dq-axis current commands; i_a^*, i_b^* and i_c^* are three-phase current commands of the DC/AC inverter for current controlled PWM; θ_i is synchronous angle obtained from the phase-lock loop based on SOGI-PLL; v_a^+, v_b^+ and v_c^+ are positive phase-sequence three-phase voltage. Moreover, P_m^* can be obtained from MPPT control algorithm of the PV system. When the voltage sag on Bus 1 shown in Fig. 1 exceeds 10%, which triggers the grid fault signal, then P_{LVRT}^* becomes the active power command and Q_{LVRT}^* is the reactive power command, which is obtained according to the E.ON grid requirements [9], [10]. Furthermore, the PV controller performs the voltage sag detection and power calculation by using the grid voltages

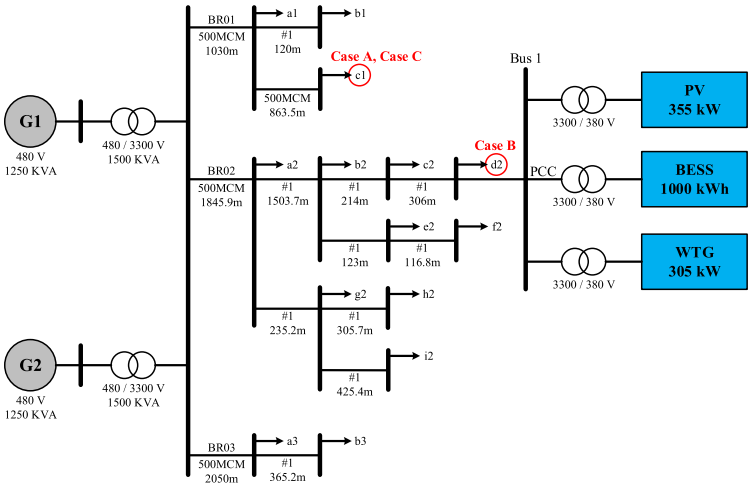

FIGURE 1. Single-line diagram of cimei Island power system.

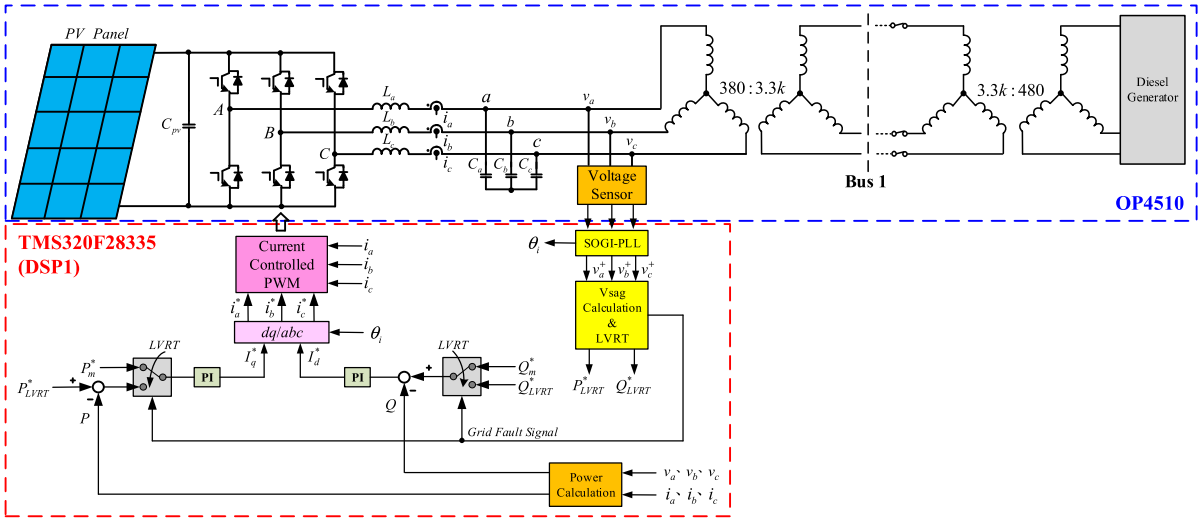

FIGURE 2. Active/reactive power control structure of PV system.

and currents. Then, the closed-loop control of the active and reactive power are achieved. After the coordinate transformation and three-phase current control, the PWM control signals are delivered to the three-phase inverter for the active and reactive power control. The required compensation reactive power command Q^*_{LVRT} is a function of the voltage sag V_{sag} and can be expressed as:

$$Q^*_{LVRT} = \begin{cases} 0, & V_{sag} < 0.1 \\ Q_{max}, & V_{sag} > 0.5 \\ 200V_{sag}\%Q_{max}, & 0.1 \le V_{sag} \le 0.5 \end{cases} \quad (1)$$

where Q_{max} equals to the maximum power capacity of PV system and V_{sag} is the voltage sag at the PCC reflected to low voltage side of the transformer. Since there is no LVRT requirement to clearly specify the voltage reduction ratio under the condition of unbalance three-phase voltage, the voltage sag V_{sag} at the PCC can be evaluated as follows [38]:

$$V_{sag} = 1 - \frac{\left|V_p^+\right|}{V_{base}} pu \quad (2)$$

$$\left|V_p^+\right| = \sqrt{\frac{1}{3}\left(v_a^{+2} + v_b^{+2} + v_c^{+2}\right)} \quad (3)$$

where V_p^+ represents the peak value of the positive sequence of three-phase voltage and V_{base} is the peak value of the nominal phase voltage of PV system, which equals 310 V in this study. Accordingly, equation (2) can also be applied to voltage reduction ratio for the balance three-phase voltage.

The active/reactive power control and VRC structure of BESS system is shown in Fig. 3. P^*_{BS} and P_{BS} are the active power command and active power; Q^*_{BS} and Q_{BS} are the reactive power command and reactive power; v_{ao}, v_{bo} and v_{co} are three-phase voltages; i_{ao}, i_{bo} and i_{co} are three-phase currents; I^*_{dm}, I^*_{qm} and I_{do}, I_{qo} are dq-axis current commands

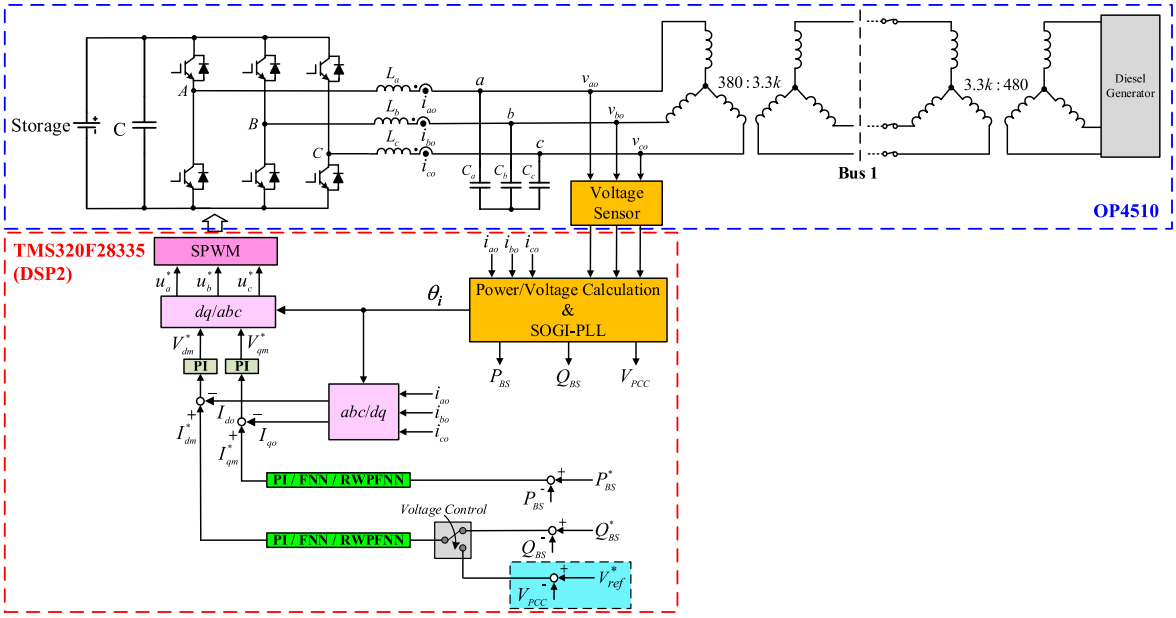

FIGURE 3. Active/reactive power control and VRC structure of BESS.

and dq-axis currents; V_{dm}^* and V_{qm}^* are dq-axis SPWM voltage commands of the DC/AC inverter; θ_i is synchronous angle obtained from the PLL; u_a^*, u_b^* and u_c^* are three-phase voltage commands of the DC/AC inverter for SPWM; V_{PCC} is the instantaneous voltage at the PCC reflected to low voltage side of the transformer. In order to restore the V_{PCC} as quickly as possible, the direct voltage control is necessary instead of indirect control. Therefore, when the voltage sag on Bus 1 shown in Fig. 1 exceeds 10%, the VRC will be triggered and the voltage control is ON. Then, the command becomes V_{ref}^*, i.e., the peak value of the nominal phase voltage of 310 V, for the voltage restoration. On the other hand, since V_{PCC} will increase abruptly when the grid recovers from the grid faults, the voltage control is OFF and the command becomes Q_{BS}^* when V_{PCC} is higher than 1.03 pu. In Fig. 3, the control system processes the active and reactive power calculations by using the grid voltages and currents. After that, the closed-loop control of active/reactive power or voltage are performed. The control objective is to regulate the quantity (active power, reactive power and voltage) to follow the control command. Moreover, besides the proposed RWPFNN controller, both conventional PI controller and FNN controller are implemented in this study for the comparison of the control performance. Furthermore, to simplify the implementation of control strategy, the PI controller with fixed parameters is adopted for the inner-loop current controller. The control error and fluctuation would be compensated by the outer-loop controller, i.e., the PI, FNN, or proposed RWPFNN controller. The algorithm of the VRC is shown in Fig. 4.

The active/reactive power control structure of WTG system is shown in Fig. 5. An AC/DC converter with current controlled PWM is considered as the first stage and responsible

Voltage control algorithm	
1:	Initial value
2:	Step 1: determine the voltage sag
3:	if $V_{sag}(N) \geq 0.1$
4:	Voltage_control = ON
5:	Step 2: end of voltage control
6:	if $V_{PCC}(N) \geq 1.03\ pu$
7:	Voltage_control = OFF
8:	Step 3: voltage control/reactive power control
9:	If Voltage_control = ON
10:	$e_1(N) = V_{ref}^* - V_{PCC}(N)$
11:	$e_2(N)$ = derivative of $e_1(N)$
12:	$I_{dm}^*(N)$ = PI/FNN/RWPFNN ($e_1(N)$, $e_2(N)$)
13:	else
14:	$e_1(N) = Q_{BS}^*(N) - Q_{BS}(N)$
15:	$e_2(N)$ = derivative of $e_1(N)$
16:	$I_{dm}^*(N)$ = PI/FNN/RWPFNN ($e_1(N)$, $e_2(N)$)
17:	end

FIGURE 4. VRC algorithm of BESS during gird faults.

for transferring the power energy from the WTG terminal to the DC bus. The second stage is a DC/AC inverter and designed to dispatch the power from the DC bus to the three-phase microgrid system. In the first stage, P_m is pole number of the PMSG; V_{dc}^* and V_{dc} are the DC bus voltage command and regulated DC bus voltage; θ_m and θ_e are the rotor shaft position and flux position; i_{as}, i_{bs} and i_{cs} are sensed phase currents; I_{ds}^* and I_{qs}^* are dq-axis current commands; i_{as}^*, i_{bs}^* and i_{cs}^* are three-phase current commands of the AC/DC

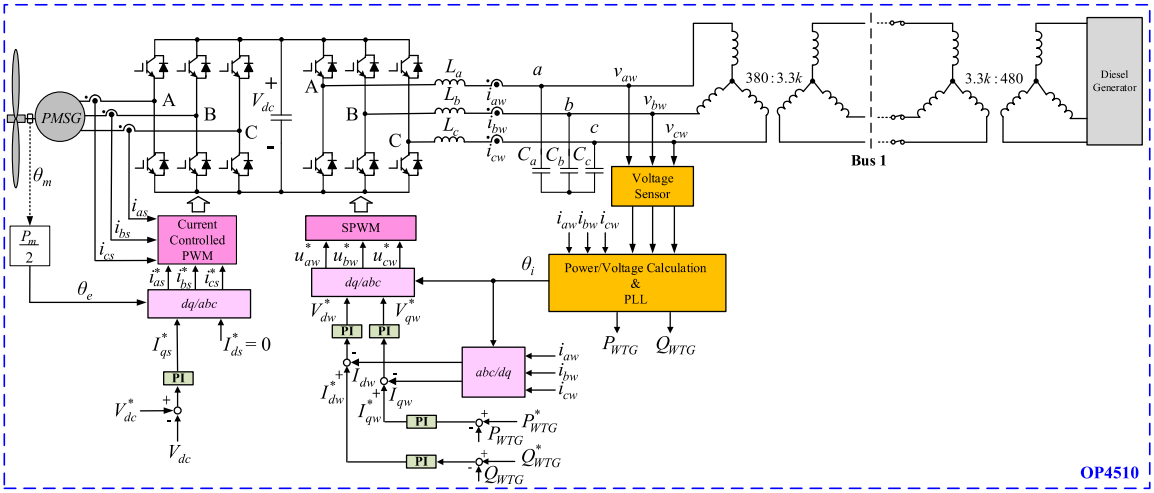

FIGURE 5. Active/reactive power control structure of WTG system.

converter. For the DC/AC inverter, it is used for active and reactive power control. P^*_{WTG} and P_{WTG} are the active power command and active power; Q^*_{WTG} and Q_{WTG} are the reactive power command and reactive power; v_{aw}, v_{bw} and v_{cw} are three-phase voltages; i_{aw}, i_{bw} and i_{cw} are three-phase currents; I^*_{dw}, I^*_{qw} and I_{dw}, I_{qw} are dq-axis current commands and dq-axis currents; V^*_{dw} and V^*_{qw} are the dq-axis SPWM voltage commands of the DC/AC inverter; θ_i is synchronous angle obtained from the PLL;u^*_{aw}, u^*_{bw} and u^*_{cw} are three-phase voltage commands of the DC/AC inverter for SPWM. The controllers of the WTG system are modeled in the OP4510 as shown in Fig. 5. Moreover, the function of LVRT is not considered in the control of the WTG in this study.

III. RWPFNN CONTROLLER

Voltage restoration by using the BESS is important to the microgrid operation during grid faults. To improve the transient control performance of VRC in a microgrid, the intelligent RWPFNN controller is designed to replace the PI controller or FNN controller in the BESS as shown in Fig. 3. The proposed RWPFNN is constructed by a five-layer network as depicted in Fig. 6, which comprises the input layer (layer i), membership layer (layer j), wavelet layer and petri layer (layer k), rule layer with recurrent structure (layer l), and output layer (layer o). The online backpropagation learning algorithm is applied to perform the parameters adaptation. In this way, the controller can maintain the robust and stable real-time control performance under the disturbances of the microgrid. The signal propagation and the fundamental function for each layer of the RWPFNN are illustrated in the following.

A. NETWORK STRUCTURE OF RWPFNN

The signal propagation and the basic function in each layer of the RWPFNN are described as follows:

1) LAYER 1: INPUT LAYER

There are two inputs in this layer, the input and the output can be defined as:

$$net_i^1(N) = x_i^1 \tag{4}$$

$$y_i^1(N) = f_i^1(net_i^1(N)) = net_i^1(N), \quad i = 1, 2 \tag{5}$$

where x_i^1 and $y_i^1(N)$ are the input and output of the ith neuron, N is the iteration index. In this study, $e_1(N) = e$ represents the error between reference command and the response. Thus, $P^*_{BS} - P_{BS}$ and $Q^*_{BS} - Q_{BS}$ represent the errors between the reference active/reactive power and instantaneous output active/reactive power of controller for the BESS in normal operation, respectively. On the other hand, the error between the reference voltage and instantaneous voltage of PCC would be $V^*_{ref} - V_{PCC}$ accordingly. Then $e_2(N) = \dot{e}$ is the derivative of error and define x_1^1 as e while x_2^1 as $\dot{e}$.

2) LAYER 2: MEMBERSHIP LAYER

The Gaussian function is adopted as the membership function to realize the fuzzification operation in each node of this layer. The input and output node of this layer are described below:

$$net_j^2(N) = -\frac{(x_i^2 - m_j^2)^2}{(\sigma_j^2)^2} \tag{6}$$

$$y_j^2(N) = f_j^2(net_j^2(N)) = \exp(net_j^2(N)), \quad j = 1, 2, \ldots, 6 \tag{7}$$

where $y_j^2(N)$ represents output of jth neuron in the membership layer; $m_j^2(N)$, $\sigma_j^2(N)$ are the mean, standard deviation of Gaussian function in the jth term associated with the input layer, respectively.

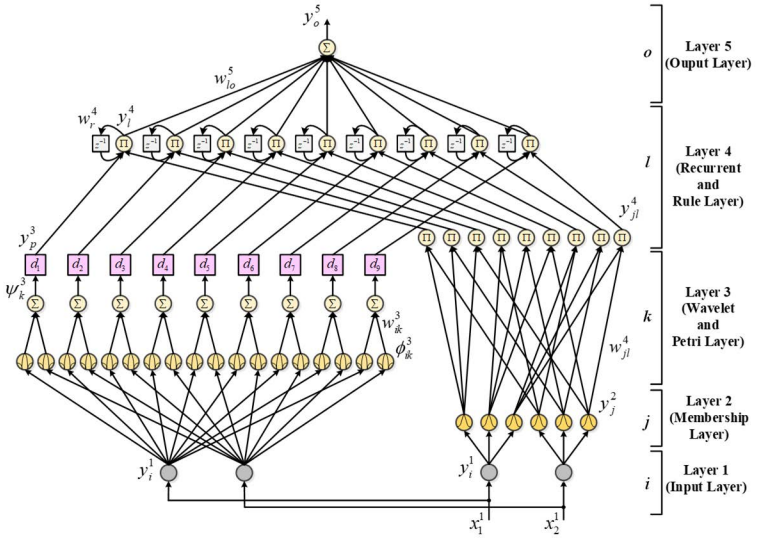

FIGURE 6. Structure of RWPFNN.

3) LAYER 3: WAVELET AND PETRI LAYER

The wavelet function in this layer can be expressed as

$$\phi_{ik}^3(N) = \frac{1}{\sqrt{|\sigma_{ik}^3|}}\left[1 - \frac{(x_i^1(N) - m_{ik}^3)^2}{(\sigma_{ik}^3)^2}\right] \exp\left[-\frac{(x_i^1(N) - m_{ik}^3)^2}{2(\sigma_{ik}^3)^2}\right], \quad k = 1, 2, ..., 9 \tag{8}$$

$$\psi_k^3(N) = \sum w_{ik}^3 \phi_{ik}^3(x) \tag{9}$$

where $\phi_{ik}^3(N)$ is the *kth* term of wavelet function output associated with the *ith* neuron, $\psi_k^3(N)$ is the summation of the *kth* term of wavelet function output, and w_{ik}^3 is the weight of wavelet layer.

Since the PN has been proven powerful for modeling and analysis of complex system, a properly designed transition function can aid the system to process the urgent events such as grid faults in order to fulfill requirements [30]. In this layer, the transition of node starts when the token is created in the input place. Then, it is controlled to activate or cancel the transition through the following equations:

$$t_p^3(N) = \begin{cases} 1, & \psi_k^3(N) \geq d_{th} \\ 0, & \psi_k^3(N) < d_{th} \end{cases} \quad th = 1, 2, \ldots, 9 \tag{10}$$

$$d_{th} = \begin{cases} \dfrac{\alpha \exp(-\beta V)}{1 + \exp(-\beta V)}, & \textit{reference command} \geq 0 \\ \alpha - \dfrac{\alpha \exp(-\beta V)}{1 + \exp(-\beta V)}, & \textit{reference command} < 0 \end{cases} \tag{11}$$

where $t_p^3(N)$ is the transition state, d_{th} is the threshold value which is determined by the function $V{=}(e + \dot{e})/2$, α and β are positive constants. Once the error e and the derivative of error $\dot{e}$ have the trend to increase, the threshold value is lower causing the transition easier to happen; otherwise the threshold value tends to become higher trying to prevent the transition. When the transition is activated, the token can be moved from the input place to the output place. Hence, the relationship between input and output can be given as follows.

$$net_p^3(N) = \begin{cases} \psi_k^3(N), & t_p^3(N) = 1 \\ 0, & t_p^3(N) = 0 \end{cases} \tag{12}$$

$$y_p^3(N) = f_p^3(net_p^3(N)) = net_p^3(N), \quad p = 1, 2, \ldots, 9 \tag{13}$$

where $y_p^3(N)$ is the output of *pth* neuron.

4) LAYER 4: RECURRENT AND RULE LAYER

The first part of this layer is to multiply the outputs of layer 2, y_j^2. For the neuron $y_{jl}^4(N)$, the output can be expressed as

$$y_{jl}^4(N) = \prod_j w_{jl}^4 y_j^2, \quad l = 1, 2, \ldots, 9 \tag{14}$$

where w_{jl}^4 is the weight between the *jth* neuron in the membership layer and the *lth* neuron in the rule layer, which is set to be 1 in this study. Then, $y_{jl}^4(N)$ is multiplied with its recurrent part and the output of layer 3 $y_p^3(N)$ as follows:

$$net_l^4(N) = y_{jl}^4 y_p^3 w_r^4 y_l^4(N-1) \tag{15}$$

$$y_l^4(N) = f_l^4(net_l^4(N)) = net_l^4(N) \tag{16}$$

where $y_l^4(N)$ is the output of *lth* neuron in the rule layer. Since a recurrent structure is able to store the previous data of the network by capturing the past dynamic behavior of the system, it will enhance the computational strength and the generalization ability of RWPFNN and hence is more appropriate in dealing with the control of non-linear complex systems [33], [34].

5) LAYER 5: OUTPUT LAYER

In the output layer, the defuzzification is implemented with

$$net_o^5(N) = \sum_{l=1}^{9} w_{lo}^5 y_l^4(N), \quad o = 1 \tag{17}$$

$$y_o^5(N) = f_o^5(net_o^5(N)) = net_o^5(N) \tag{18}$$

where w_{lo}^5 is the weight between layer 4 and layer 5, and $y_o^5(N)$ is the output of RWPFNN. In this study, $y_o^5(N) = I_{qm}^*$ is used for the active power control and $y_o^5(N) = I_{dm}^*$ is used for the reactive power/voltage control.

B. ONLINE LEARNING ALGORITHM FOR RWPFNN

The online BP learning algorithm is based on the supervised gradient descent method to update the connected weights and the network parameters in the RWPFNN adaptively. For the reactive power control of BESS in normal operation, the objective function $E(N)$ can be defined as

$$E(N) = \frac{1}{2}\left(Q_{BS}^*(N) - Q_{BS}(N)\right)^2 = \frac{1}{2}e(N)^2 \tag{19}$$

where $e(N)$, which is $Q_{BS}^*(N) - Q_{BS}(N)$, represents the tracking error in the learning process of the RWPFNN controller for each discrete time N, with Q_{BS}^* and Q_{BS} represent the reference reactive power and the instantaneous output reactive power. In layer 5, the error term to be propagated is given by

$$\delta_o^5 = -\frac{\partial E}{\partial y_o^5(N)} = -\frac{\partial E}{\partial Q_{BS}}\frac{\partial Q_{BS}}{\partial y_o^5(N)} \tag{20}$$

The weight $w_{lo}^5(N)$ between the rule layer and output layer can be updated by the following amount.

$$\begin{aligned}\Delta w_{lo}^5 &= -\eta_{lo}\frac{\partial E}{\partial w_{lo}^5} \\ &= -\eta_{lo}\frac{\partial E}{\partial y_o^5(N)}\frac{\partial y_o^5(N)}{\partial w_{lo}^5(N)} = \eta_{lo}\delta_o^5 y_l^4 \end{aligned} \tag{21}$$

$$w_{lo}^5(N+1) = w_{lo}^5(N) + \Delta w_{lo}^5 \tag{22}$$

where η_{lo} is the learning rate.

Two error terms are necessary to be propagated in layer 4, as listed in (23) and (24) as follows:

$$\delta_l^4 = -\frac{\partial E}{\partial y_l^4(N)} = -\left[\frac{\partial E}{\partial y_o^5(N)}\right]\frac{\partial y_o^5(N)}{\partial y_l^4(N)} = \delta_o^5 w_{lo}^5 \tag{23}$$

$$\delta_{jl}^4 = -\frac{\partial E}{\partial y_{jl}^4(N)} = -\left[\frac{\partial E}{\partial y_o^5(N)}\frac{\partial y_o^5(N)}{\partial y_l^4(N)}\right]\frac{\partial y_l^4(N)}{\partial y_{jl}^4(N)} = \delta_l^4 y_p^3 \tag{24}$$

By adopting the chain rule, the connective weight Δw_r^4 for recurrent feedback can be computed by the following equation:

$$\begin{aligned}\Delta w_r^4 &= -\eta_r\frac{\partial E}{\partial w_r^4} \\ &= -\eta_r\left[\frac{\partial E}{\partial y_o^5(N)}\frac{\partial y_o^5(N)}{\partial y_l^4(N)}\right]\frac{\partial y_l^4(N)}{\partial w_r^4(N)} \\ &= \eta_r\delta_l^4 y_p^3 y_{jl}^4 y_l^4(N-1) \end{aligned} \tag{25}$$

$$w_r^4(N+1) = w_r^4(N) + \Delta w_r^4 \tag{26}$$

The error term to be propagated in layer 3 can be expressed as:

$$\begin{aligned}\delta_k^3 &= -\frac{\partial E}{\partial y_p^3(N)} \\ &= -\left[\frac{\partial E}{\partial y_o^5(N)}\frac{\partial y_o^5(N)}{\partial y_l^4(N)}\right]\frac{\partial y_l^4(N)}{\partial y_p^3(N)} = \delta_l^4 y_{jl}^4 w_r^4 y_l^4(N-1) \end{aligned} \tag{27}$$

Accordingly, the weight $w_{ik}^3(N)$ can be updated by the following amount:

$$\begin{aligned}\Delta w_{ik}^3 &= -\eta_{ik}\frac{\partial E}{\partial w_{ik}^3} \\ &= -\eta_{ik}\frac{\partial E}{\partial y_o^5(N)}\frac{\partial y_o^5(N)}{\partial y_l^4(N)}\frac{\partial y_l^4(N)}{\partial y_p^3(N)}\frac{\partial y_p^3(N)}{\partial w_{ik}^3(N)} = \eta_{ik}\delta_k^3\varphi_{ik}^3 \end{aligned} \tag{28}$$

where η_{ik} is the learning rate of weight $w_{ik}^3(N)$. Therefore, the weight $w_{ik}^3(N)$ can be updated with:

$$w_{ik}^3(N+1) = w_{ik}^3(N) + \Delta w_{ik}^3 \tag{29}$$

In layer 2, the error term needs to be propagated as:

$$\begin{aligned}\delta_j^2 &= -\frac{\partial E}{\partial net_j^2} \\ &= -\left[\frac{\partial E}{\partial y_o^5(N)}\frac{\partial y_o^5(N)}{\partial y_{jl}^4(N)}\right]\frac{\partial y_{jl}^4(N)}{\partial y_j^2(N)}\frac{\partial y_j^2(N)}{\partial net_j^2(N)} = \sum_{jl}\delta_{jl}^4 y_{jl}^4 \end{aligned} \tag{30}$$

The mean of the Gaussian function m_j^2 is calculated in the following:

$$\begin{aligned}\Delta m_j^2 &= -\eta_m\frac{\partial E}{\partial m_j^2} = -\eta_m\left[\frac{\partial E}{\partial y_o^5(N)}\frac{\partial y_o^5(N)}{\partial net_j^2(N)}\right]\frac{\partial net_j^2(N)}{\partial m_j^2(N)} \\ &= \eta_m\delta_j^2\frac{2(x_i^2 - m_j^2)}{\left(\sigma_j^2\right)^3} \end{aligned} \tag{31}$$

where η_m is the learning-rate factor of the mean of the Gaussian function. The standard deviation of the Gaussian function σ_j^2 can be calculated as below:

$$\begin{aligned}\Delta\sigma_j^2 &= -\eta_\sigma\frac{\partial E}{\partial \sigma_j^2} = -\eta_\sigma\left[\frac{\partial E}{\partial y_o^5(N)}\frac{\partial y_o^5(N)}{\partial net_j^2(N)}\right]\frac{\partial net_j^2(N)}{\partial \sigma_j^2(N)} \\ &= \eta_\sigma\delta_j^2\frac{2(x_i^2 - m_j^2)^2}{\left(\sigma_j^2\right)^3} \end{aligned} \tag{32}$$

where η_σ is the learning-rate factor of the standard deviation of the Gaussian function. The means and standard deviations of the Gaussian function are updated as follows:

$$m_j^2(N+1) = m_j^2(N) + \Delta m_j^2 \tag{33}$$

$$\sigma_j^2(N+1) = \sigma_j^2(N) + \Delta\sigma_j^2 \tag{34}$$

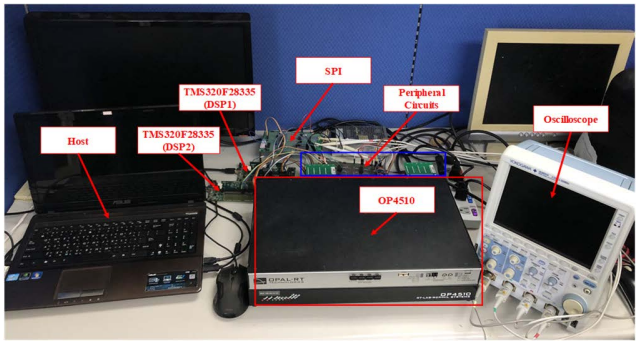

FIGURE 7. Experimental setup.

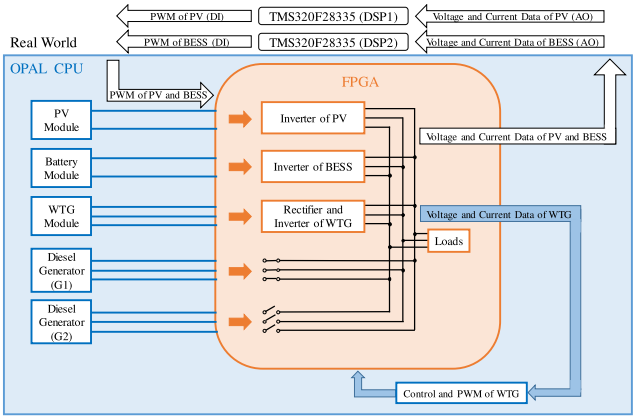

FIGURE 8. Structure of OPAL-RT and peripherals.

Owing to the uncertainties in the microgrid system, the exact Jacobian calculation, which is $\partial Q_{BS}/\partial y_o^5(N)$, is difficult to determine accurately. To solve this problem and speed up the online updating of weights, the error adaptation law proposed in [38] is adopted in this study to replace the Jacobian term with:

$$\delta_o^5 \cong e + \dot{e} \tag{35}$$

where $\dot{e}$ is the derivative of error e. In addition, to guarantee the convergence of the proposed RWPFNN controller, specific learning-rate factors for the training of the parameters of the RWPFNN are designed in the Appendix to guarantee the convergence of the tracking errors.

IV. DESIGN AND EXPERIMENTATION

The experimental setup of the proposed control strategies is shown in Fig. 7. The test platform includes the HIL mechanism built with OPAL-RT real-time simulator OP4510 and RT-LAB environment, an oscilloscope, a host computer, peripheral circuits and two DSP TMS320F28335 control boards. There are two 16-channel digital-to-analog converter modules (OP5330), one 16-channel analog-to-digital converter module (OP5340), and one 32-channel digital signal conditioning module (OP5353) in the OP4510. The PI, FNN, and proposed RWPFNN controllers of BESS are realized using the C language on the Texas Instruments TMS320F28335 DSP and the observation signals are transferred to the oscilloscope with the SPI. Moreover, 2, 6, 9, 9, 9, 1 nodes are designed in the input layer, membership layer, wavelet layer, Petri layer, rule layer, and output layer, respectively, of the RWPFNN. The structure of OPAL-RT and peripherals are shown in Fig. 8. The entire Cimei Island microgrid except the PV and BESS controllers is modeled in the host and transferred to the OP4510 with Ethernet. The controllers of the PV and BESS are modeled in two dedicated DSPs. Furthermore, as shown in Fig. 8, the microgrid with the inverters of the PV and BESS are modeled in FPGA of the OP4510, and the PV, battery, WTG modules with the diesel generators are modeled in the CPU of the OP4510. For the following three test cases shown in IV.A, IV.B and IV.C, the simulation time steps of OP4510 FPGA are 9.3×10^{-7}, 8.55×10^{-7} and 9.3×10^{-7} s, respectively, and the simulation time steps of the OP4510 CPU are both 3.125×10^{-5} s. In addition, the sampling time of the control algorithms of the PV and BESS is 1 ms and the switching frequency of the PWM is 16 kHz for both the inverters of the PV and BESS. Additionally, the flowchart of the proposed RWPFNN controller for the reactive power/voltage restoration and active power control of BESS is provided in Fig. 9 and described as follows:

1) RWPFNN Input Layer: The analog three-phase voltages v_{ao}, v_{bo} and v_{co} and the three-phase currents i_{ao}, i_{bo} and i_{co} of the microgrid are measured for the power calculation and synchronization. Then, the tracking error $e_1(N) = e$ is generated and sent to the proposed RWPFNN controller. The input variables of the proposed RWPFNN are e and $\dot{e}$; the node outputs are $y_i^1(N)$ and sent to the membership layer.

2) RWPFNN Membership Layer: The Gaussian functions are adopted to implement the fuzzification operation and the outputs are $y_j^2(N)$. Then, the outputs $y_j^2(N)$ are sent to the recurrent and rule layer..

3) RWPFNN Wavelet and Petri Layer: The wavelet layer includes k wavelet functions. The input variables of this layer are e and $\dot{e}$. Then, the node outputs $\psi_k^3(N)$ are obtained by performing the summation and multiplying operations and sent to the PN. When the transition is activated, the token can be moved from the input place to the output place. The outputs are $y_p^3(N)$ and sent to the recurrent and rule layer.

4) RWPFNN Recurrent and Rule Layer: This layer contains the recurrent and rule layers. The nodes of the rule layer multiply the output signals from the membership layer, the wavelet and petri layer and recurrent layer. The outputs are $y_l^4(N)$ and sent to the output layer.

5) RWPFNN Output Layer: The node performs the summation operation for the output $y_o^5(N)$. Moreover, the output $y_o^5(N)$ of the proposed RWPFNN is the current command I_{dm}^* of BESS for the reactive power control/VRC and the current command I_{qm}^* of BESS for active power control, respectively.

6) Online Network Parameters Learning Using BP: The online parameters learning is achieved by online tuning of the connective weights w_{lo}^5 between the output layer and the

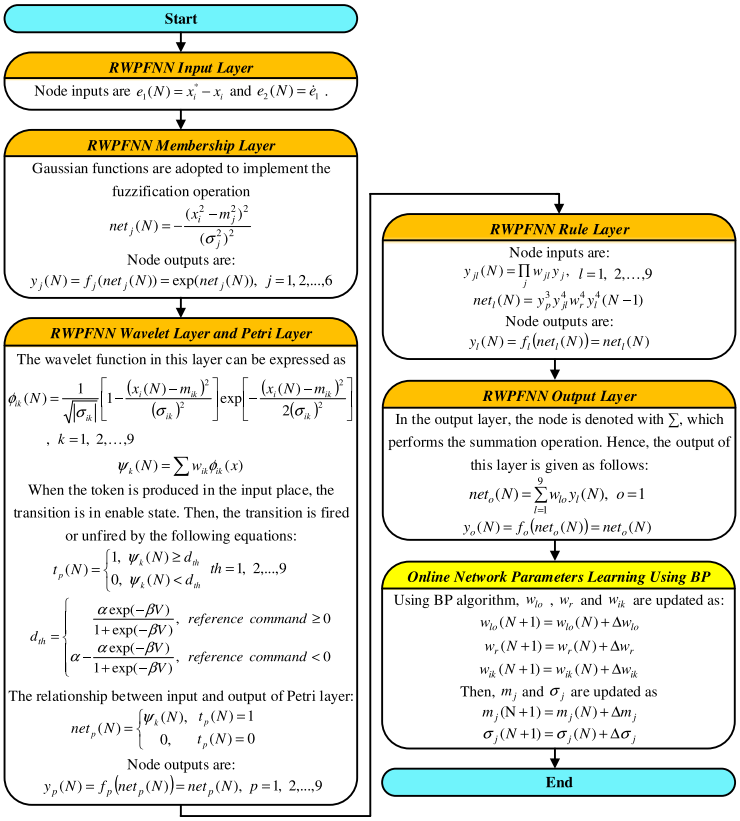

FIGURE 9. Flowchart of the proposed RWPFNN controller in DSP.

rule layer, the recurrent connective weights w_r^4, the connective weights w_{ik}^3 in the wavelet and petri layer, and the mean m_j^2 and standard deviations σ_j^2 of the membership functions in the membership layer using the BP algorithm.

All the PI, FNN and RWPFNN controllers are coded in the current control loop with 1ms sampling time. Since the clock rate of the adopted DSP TMS320F28335 is 150MHz, the operation cycles and execution time of the PI, FNN and RWPFNN controllers are 179 cycles (1.1933 μs), 1612 cycles (10.7467 μs) and 15214 cycles (101.4267 μs), respectively. Though the proposed RWPFNN controller is more complicated than both PI and FNN, the execution time is still within the 1ms sampling time of the current control loop with the same hardware environment.

To evaluate the control performance of the mentioned controllers, the IAE index and the response time during the grid faults, and the MAE index after the restoration of the grid faults are listed in (36), (37) and (38) as follows:

$$\text{IAE} = \int_{t1}^{t4} |e(t)|\, dt \tag{36}$$

$$\text{Response time} = t2 - t1 \tag{37}$$

$$\text{MAE} = (|e(t)|),\ t \in [t3, t5] \tag{38}$$

where the time parameters of performance measurings can be found in Table 1.

TABLE 1. Time parameters of performance measurings.

Time Parameters	Definition
t1	Beginning of grid fault
t2	Response time to achieve steady state of reference command during grid fault
t3	End of grid fault
t4	End of voltage control
t5	1 s

Due to the short-circuit current of the diesel generator is rising rapidly, which may exceed the maximum short-circuit capacity of the diesel generator, a three-phase FCL circuit is adopted to limit the excess current in this study. FCLs are proper means for reducing fault current level in the microgrid system. Considering that a large inductor can present extremely large impedance to system with high frequency component, the inductive FCLs, compared with its resistive counterpart, are very effective in restricting the rising speed of the short-circuit current of the diesel generator which may cause major damage during the grid faults [39]–[41]. Therefore, a three-phase inductive FCL is connected in series with the diesel generator and the microgrid system as shown in Fig. 10. In the simulation, the FCL impedances, Z_{FCL}, are obtained via trial and error considering the requirements of maximum capacity of the diesel generator and the system

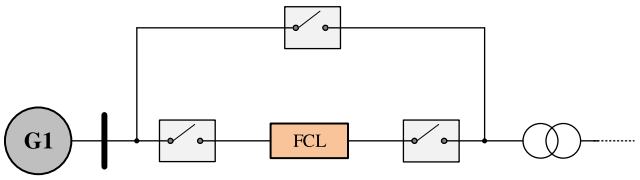

FIGURE 10. Single-line diagram of diesel generator with FCL.

stability. The result is:

$$Z_{FCL} = 0.05\Omega + 0.05\ mH \tag{39}$$

As shown in Fig. 10, the FCL is disconnected from the system in normal operation. On the other hand, the FCL is connected in series with the power line and diesel generator during grid faults in order to reduce the fault current from exceeding the maximum capacity of the diesel generator and enhance the stability of the microgrid system.

In the following, Case A and Case B two test cases at heavy load and light load with grid fault for the Cimei Island microgrid are designed to consider the effect of parameter uncertainties and external disturbances on the control performance of the microgrid and examine the transient responses of the PI, FNN and proposed RWPFNN controllers for the VRC of BESS and the compliance with the E.ON standard of the LVRT for the PV. Moreover, Case C is designed to further investigate the effect of variations in power output of PV and wind turbine on performance.

A. FAULT OCCURS AT HEAVY LOAD WITH BESS IN DISCHARGING MODE

In Case A, the PV, WTG and BESS all output power to supply the loads. A three-phase short-circuit and grounding fault occurs in c1 of the microgrid as shown in Fig. 1 causing the voltage sag with 16.15% drop at the PCC. The resistance of grounding fault is set to be 8.63 Ω. In the beginning, the microgrid is in normal operation with No. 1 diesel generator (G1) operating with loads 956.34 kW and 314.31 kVar. The PV system outputs 300 kW and the WTG outputs 305 kW. The control command for the BESS is in the discharging mode with 300 kW as shown in Figs. 11, 12 and 13. In this way, the diesel generator would provide 51.34 kW and 341.31 kVar to support the operation of the microgrid. Due to the three-phase short-circuit and grounding fault at 0.4 s, the microgrid is facing voltage sag and the PV system, WTG system and BESS should maintain the same output power. Meanwhile, the PV system and BESS have captured the voltage sag exceeding 10%, and then output the reactive power to meet the LVRT requirements and execute VRC, respectively. At the same time, the diesel generator will increase or decrease its active and reactive power outputs to balance the load. Afterwards, the fault is removed at 0.6 s, the microgrid restores to the normal operation. The voltage responses of voltage sag without LVRT and VRC and voltage restoration with LVRT and VRC of the PI, FNN and proposed RWPFNN controllers are in Figs. 11(a), 12(a) and 13(a). All three controllers can achieve the nominal phase voltage of 310 V owing to the reactive power outputs of the BESS. The active and reactive power outputs of the PV system with PI, FNN and RWPFNN controllers are shown in Figs. 11(b), 12(b) and 13(b). According to the E.ON standard of 16.15% drop, the reactive power outputs of PV system should be above 90.37 kVar. Owing to the VRC, the required reactive power outputs of PV of all the controllers are well below 90.37 kVar, which are compensated with the reactive power output of BESS. Moreover, thanks to the fast transient response of RWPFNN controller of BESS, the required reactive power output of PV is the smallest among three controllers. Furthermore, the active and reactive power outputs of BESS of the PI, FNN and RWPFNN controllers are shown in Figs. 11(c), 12(c) and 13(c). The control commands and signals of the BESS are shown in Figs. 11(d), 12(d) and 13(d), respectively. From the experimental results, though good transient voltage response can be obtained by using the PI controller, the voltage error is large and will degrade the voltage restoration performance of the microgrid system. On the other hand, owing to the parallel computation and online learning capabilities of FNN, the voltage error is reduced comparing with the PI controllers. In addition, since the proposed RWPFNN combines the merits of the functional advantages of the PN, RFNN and WFNN, the voltage error is much reduced.

TABLE 2. Performance measurings of various controllers on voltage restoration and active power control at heavy load.

Controllers / Measurings	Experimentation					
	PI		FNN		RWPFNN	
	V_{PCC}	P_{BS}	V_{PCC}	P_{BS}	V_{PCC}	P_{BS}
IAE	3.061	6.17	2.898	4.92	2.689	3.95
Response time (s)	0.179	0.2	0.147	0.181	0.105	0.161
MAE	87	66	80	60	76	58

The performance measurings of the PI, FNN and RWPFNN controllers with VRC and active power control of BESS at heavy load are compared in Table 2. From Table 2, the IAE, the response time and the MAE of voltage restoration of the proposed RWPFNN controller are lower than both the PI and FNN controllers. Moreover, the IAE, the response time and the MAE of active power control of the proposed RWPFNN controller are still the lowest among three controllers.

B. FAULT OCCURS AT LIGHT LOAD WITH BESS IN CHARGING MODE

In Case B, the PV and WTG output power to supply the loads with BESS in charging mode. A three-phase short-circuit and grounding fault occurs in d2 of the microgrid as shown in Fig. 1 causing the voltage sag with 26.47% drop at the PCC. The resistance of grounding fault is set to be 13 Ω. In the beginning, the microgrid is in normal operation with No. 1 diesel generator (G1) operating with loads 680.25 kW

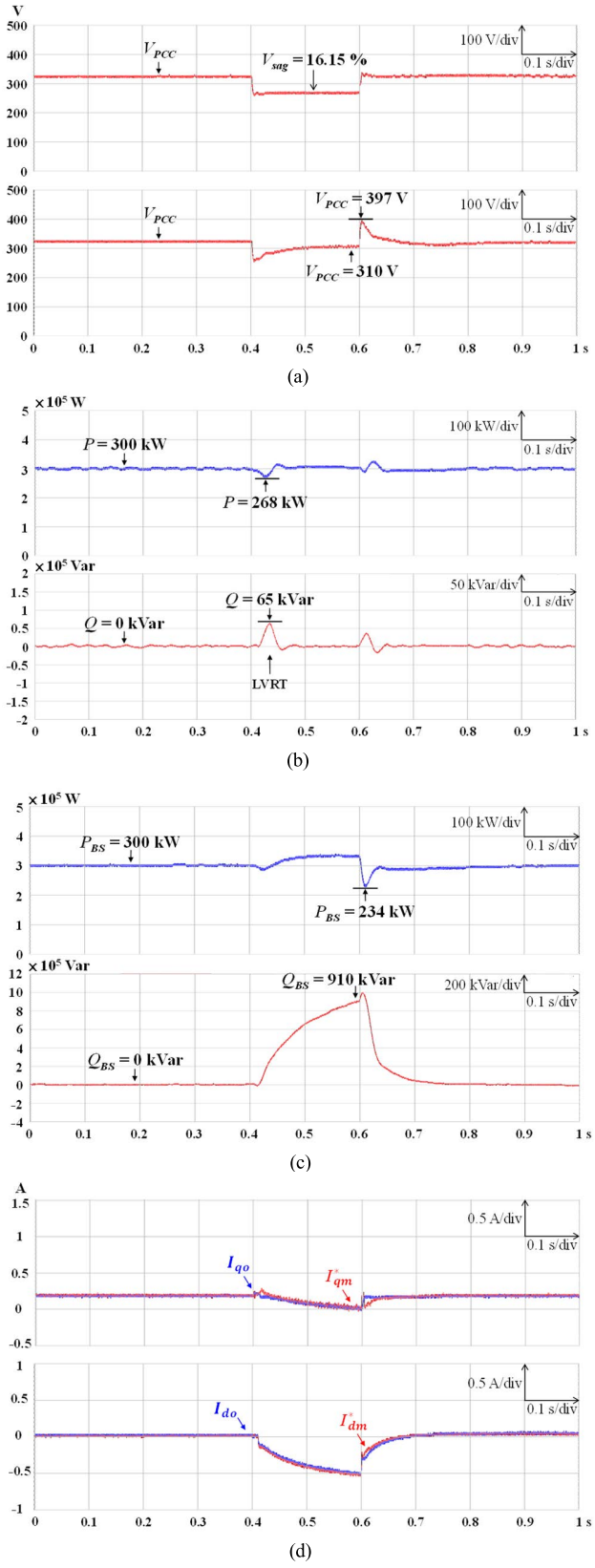

FIGURE 11. Various responses of PI controller at heavy load. (a) Voltage sag and voltage restoration of V_{PCC}, (b) P and Q of PV, (c) P_{BS} and Q_{BS} of BESS, (d) I^*_{qm}, I_{qo} and I^*_{dm}, I_{do} of BESS.

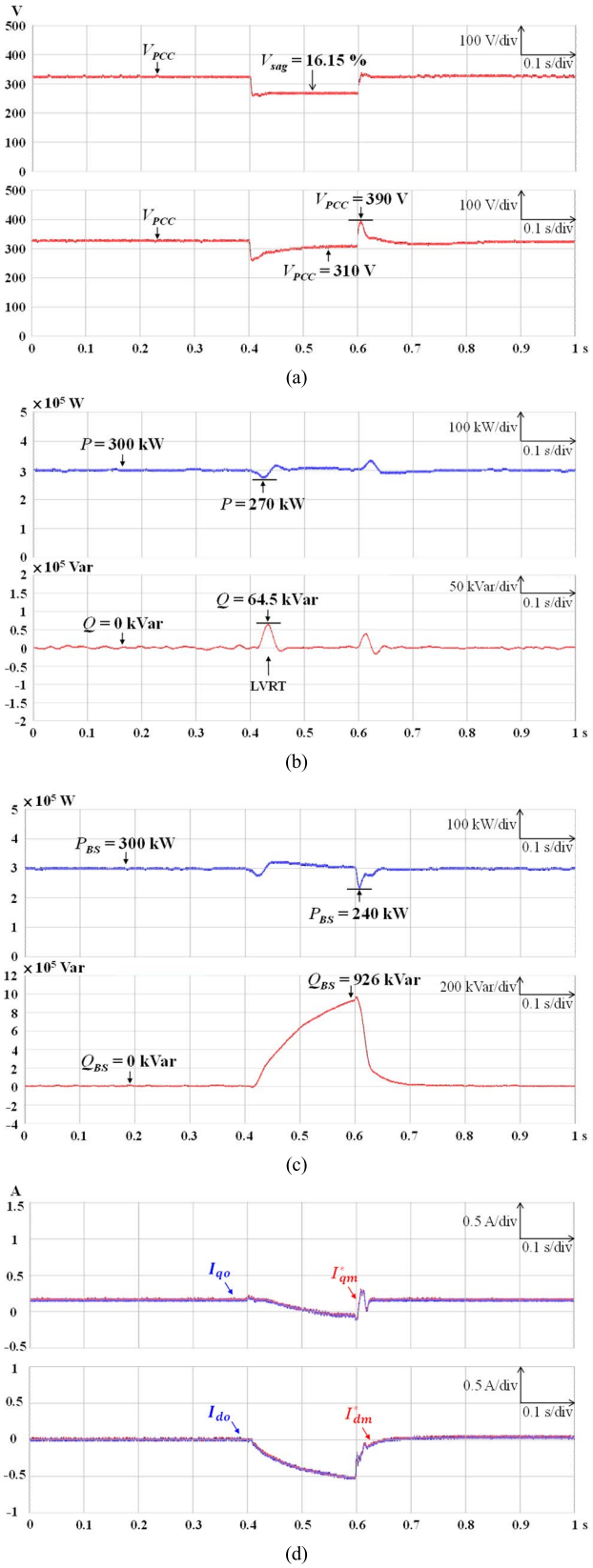

FIGURE 12. Various responses of FNN controller at heavy load. (a) Voltage sag and voltage restoration of V_{PCC}, (b) P and Q of PV, (c) P_{BS} and Q_{BS} of BESS, (d) I^*_{qm}, I_{qo} and I^*_{dm}, I_{do} of BESS.

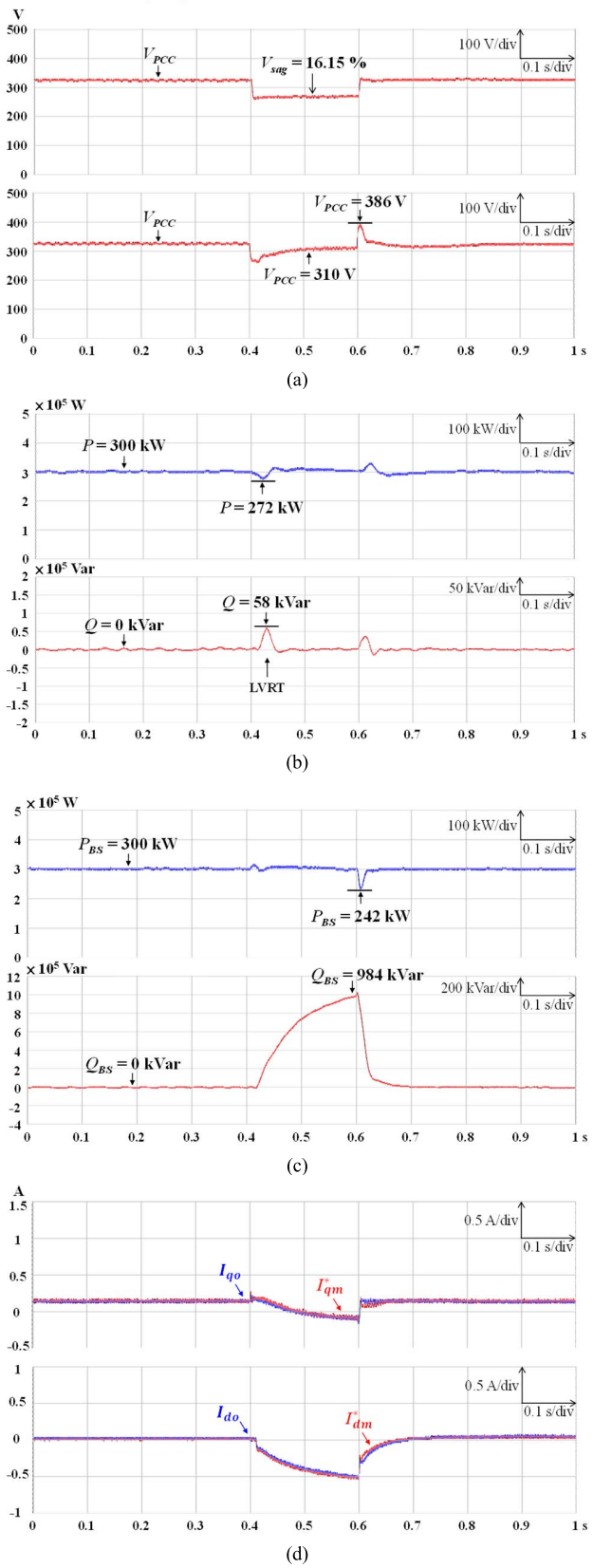

FIGURE 13. Various responses of RWPFNN controller at heavy load. (a) Voltage sag and voltage restoration of V_{PCC}, (b) P and Q of PV, (c) P_{BS} and Q_{BS} of BESS, (d) I^*_{qm}, I_{qo} and I^*_{dm}, I_{do} of BESS.

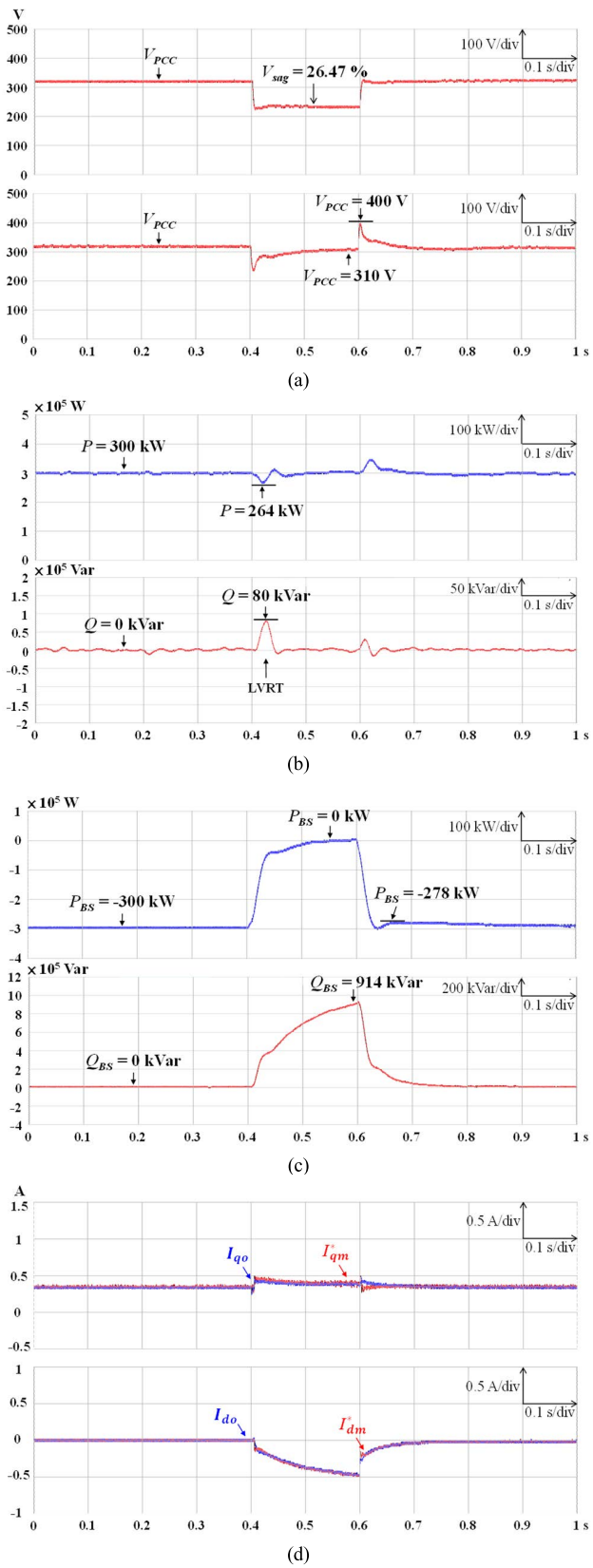

FIGURE 14. Various responses of PI controller at light load. (a) Voltage sag and voltage restoration of V_{PCC}, (b) P and Q of PV, (c) P_{BS} and Q_{BS} of BESS, (d) I^*_{qm}, I_{qo} and I^*_{dm}, I_{do} of BESS.

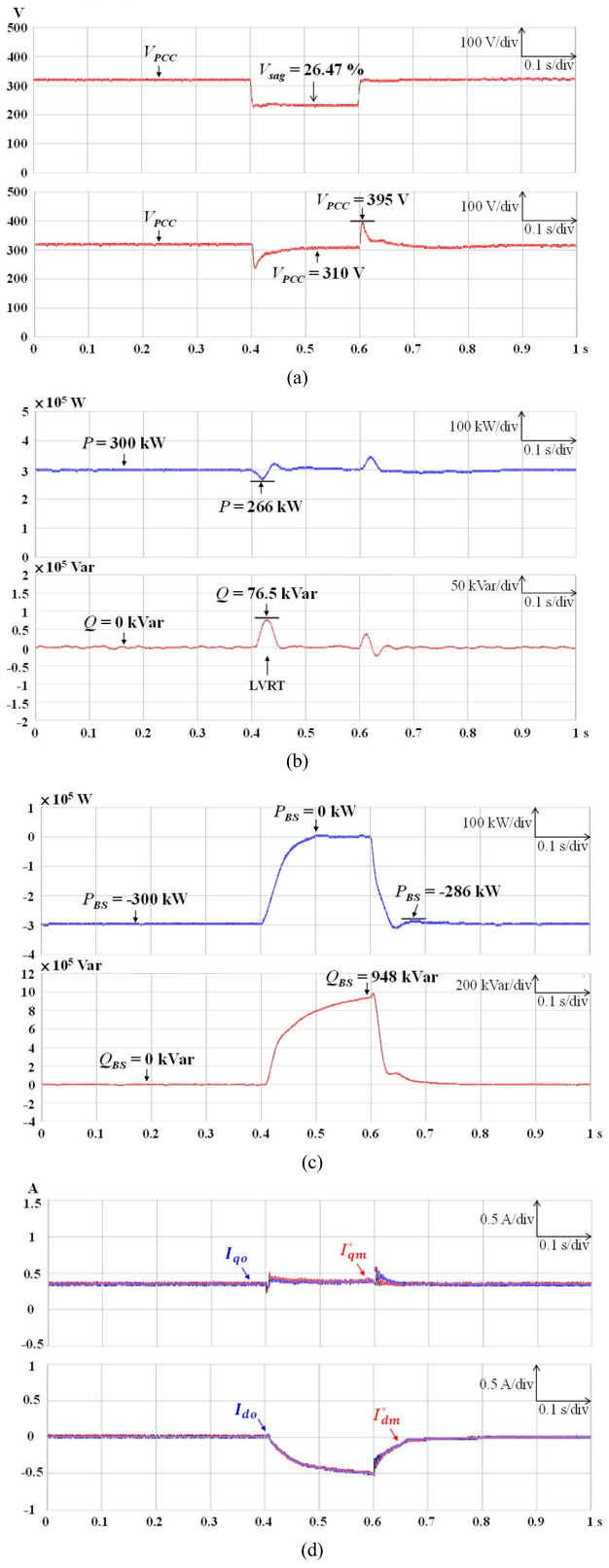

FIGURE 15. Various responses of FNN controller at light load. (a) Voltage sag and voltage restoration of V_{PCC}, (b) P and Q of PV, (c) P_{BS} and Q_{BS} of BESS, (d) I^*_{qm}, I_{qo} and I^*_{dm}, I_{do} of BESS.

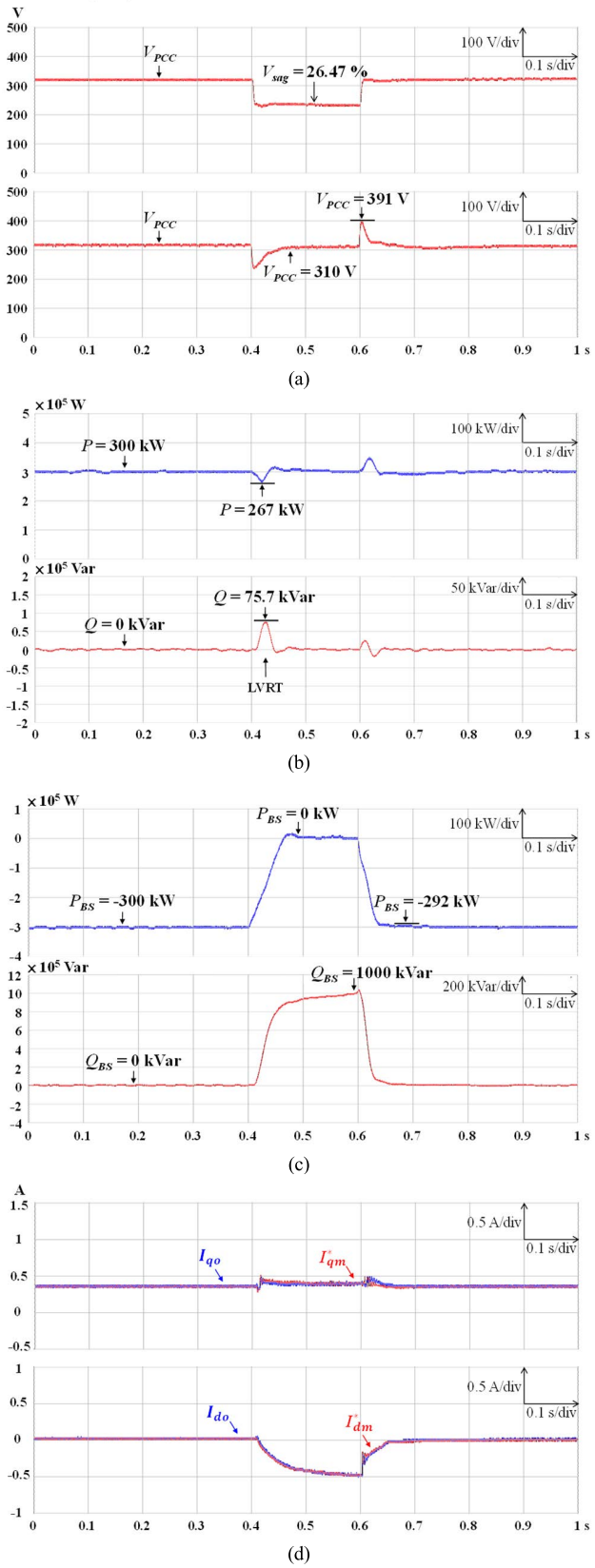

FIGURE 16. Various responses of RWPFNN controller at light load. (a) Voltage sag and voltage restoration of V_{PCC}, (b) P and Q of PV, (c) P_{BS} and Q_{BS} of BESS, (d) I^*_{qm}, I_{qo} and I^*_{dm}, I_{do} of BESS.

TABLE 3. Performance measurings of various controllers on voltage restoration and active power control at light load.

Controllers / Measurings	Experimentation					
	PI		FNN		RWPFNN	
	V_{PCC}	P_{BS}	V_{PCC}	P_{BS}	V_{PCC}	P_{BS}
IAE	3.899	10.78	3.411	8.25	3.031	7.87
Response time (s)	0.178	0.152	0.121	0.102	0.064	0.085
MAE	90	22	85	14	81	8

TABLE 4. Performance measurings of various controllers on voltage restoration and active power control in Case C.

Controllers / Measurings	Experimentation					
	PI		FNN		RWPFNN	
	V_{PCC}	P_{BS}	V_{PCC}	P_{BS}	V_{PCC}	P_{BS}
IAE	3.203	6.51	2.916	5.23	2.703	4.39
Response time (s)	0.177	0.2	0.136	0.168	0.104	0.129
MAE	88	115	84	83	75	80

and 223.51 kVar. The PV system outputs 300 kW and the WTG outputs 305 kW. The control command for the BESS is in the charging mode with 300 kW as shown in Figs. 14, 15 and 16. In this way, the diesel generator would provide 375.25 kW and 223.51 kVar to support the operation of the microgrid. Due to the three-phase short-circuit and grounding fault at 0.4 s, the microgrid is facing voltage sag with the PV system and WTG system are required to keep the same output power. Meanwhile, the BESS and PV system have captured the voltage sag exceeding 10%. Then, the BESS stops charging in order to decrease active power load of the microgrid and supply reactive power for the VRC, and the PV system also outputs reactive power to meet the LVRT requirements. Afterwards, the fault is removed at 0.6 s, the microgrid restores to the normal operation. The voltage responses of voltage sag without LVRT and VRC and voltage restoration with LVRT and VRC of the PI, FNN and proposed RWPFNN controllers are in Figs. 14(a), 15(a) and 16(a). All three controllers can achieve the nominal phase voltage of 310 V owing to the reactive power outputs of the BESS. The active and reactive power outputs of the PV system with PI, FNN and RWPFNN controllers are shown in Figs. 14(b), 15(b) and 16(b). According to the E.ON standard of 26.47% drop, the reactive power outputs of PV system should be above 149.58 kVar. Owing to the VRC, the required reactive power outputs of PV are much smaller than 149.58 kVar, which are compensated with the reactive power output of BESS. Moreover, thanks to the fast transient response of RWPFNN controller of BESS, the required reactive power output of PV is the smallest among three controllers. Furthermore, the active and reactive power outputs of BESS of the PI, FNN and RWPFNN controllers are shown in Figs. 14(c), 15(c) and 16(c). The control commands and signals of the BESS are shown in Figs. 14(d), 15(d) and 16(d). From the experimental results, both the LVRT requirements of the PV system and VRC of the BESS are fulfilled. In addition, the proposed RWPFNN controller possesses fast response with small voltage restoration error comparing with the PI and FNN controllers.

The performance measurings of the three controllers with VRC and active power control of BESS at light load are compared in Table 3. From Table 3, the IAE, the response time and the MAE of voltage restoration of the proposed RWPFNN controller are lower than both the PI and FNN controllers. Moreover, the IAE, the response time and the MAE of active power control of the proposed RWPFNN controller are the lowest as well.

C. FAULT OCCURS WITH VARIATIONS IN POWER OUTPUT OF PV AND WIND TURBINE

In Case C, the PV, WTG and BESS all output power to supply the loads with the PV system changing its output to 330 kW (+30 kW) and the WTG system changing its output to 275 kW (−30 kW) abruptly at 0.4 s, while the rest of the conditions are the same as Case A to further consider the effect of variations in power output of PV and wind turbine on performance. A three-phase short-circuit and grounding fault occurs in c1 of the microgrid as shown in Fig. 1 causing the voltage sag with 16.25% drop at the PCC. The resistance of grounding fault is set to be 8.63 Ω. In the beginning, the microgrid is in normal operation with No. 1 diesel generator (G1) operating with loads 956.34 kW and 314.31 kVar. The PV system outputs 300 kW and the WTG outputs 305 kW. The control command for the BESS is in the discharging mode with 300 kW as shown in Figs. 17, 18 and 19. In this way, the diesel generator would provide 51.34 kW and 341.31 kVar to support the operation of the microgrid. Due to the three-phase short-circuit and grounding fault with the PV system changing its output to 330 kW and the WTG system changing its output to 275 kW abruptly at 0.4 s, the microgrid is facing voltage sag and BESS should maintain the same output power. Meanwhile, the PV system and BESS have captured the voltage sag exceeding 10%, and then output the reactive power to meet the LVRT requirements and execute VRC, respectively. At the same time, the diesel generator will increase or decrease its active and reactive power outputs to balance the load. Afterwards, the fault is removed at 0.6 s, the microgrid restores to the normal operation. The voltage responses of voltage sag without LVRT and VRC and voltage restoration with LVRT and VRC of the PI, FNN and proposed RWPFNN controllers are in Figs. 17(a), 18(a) and 19(a). All three controllers can achieve the nominal phase voltage of 310 V owing to the reactive power outputs of the BESS. The active and reactive power outputs of the PV system with PI, FNN and RWPFNN controllers are shown in Figs. 17(b), 18(b) and 19(b). According to the E.ON standard of 16.25% drop, the reactive power outputs of PV system should be above 94.25 kVar. Owing to the VRC, the required reactive power outputs of PV of all the controllers are well below 94.25 kVar, which are compensated with

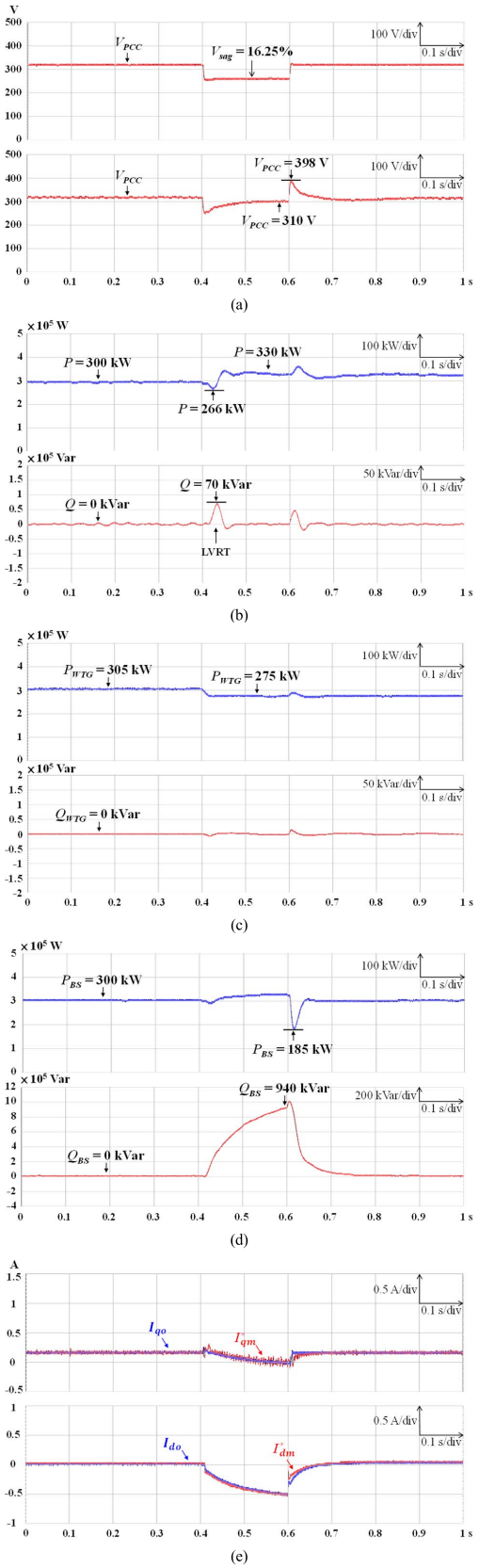

FIGURE 17. Various responses of PI controller in Case C. (a) Voltage sag and voltage restoration of V_{PCC}, (b) P and Q of PV, (c) P_{WTG} and Q_{WTG} of WTG, (d) P_{BS} and Q_{BS} of BESS, (e) I^*_{qm}, I_{qo} and I^*_{dm}, I_{do} of BESS.

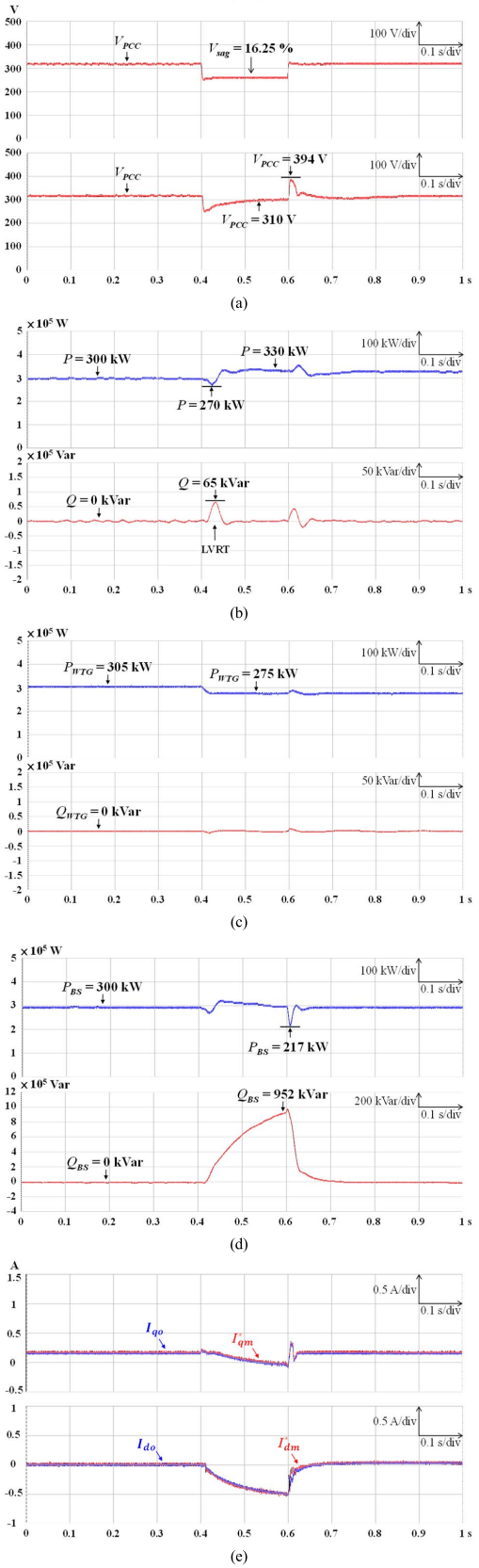

FIGURE 18. Various responses of FNN controller in Case C. (a) Voltage sag and voltage restoration of V_{PCC}, (b) P and Q of PV, (c) P_{WTG} and Q_{WTG} of WTG, (d) P_{BS} and Q_{BS} of BESS, (e) I^*_{qm}, I_{qo} and I^*_{dm}, I_{do} of BESS.

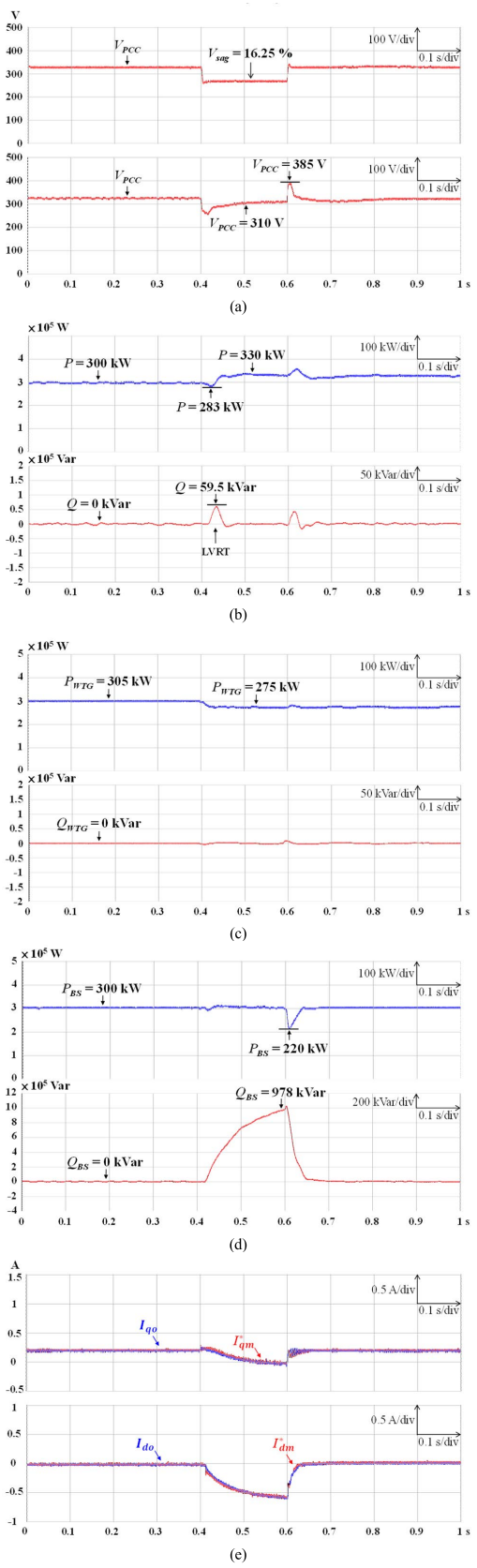

FIGURE 19. Various responses of RWPFNN controller in Case C. (a) Voltage sag and voltage restoration of V_{PCC}, (b) P and Q of PV, (c) P_{WTG} and Q_{WTG} of WTG, (d) P_{BS} and Q_{BS} of BESS, (e) I_{qm}^*, I_{qo} and I_{dm}^*, I_{do} of BESS.

the reactive power output of BESS. Moreover, thanks to the fast transient response of RWPFNN controller of BESS, the required reactive power output of PV is the smallest among three controllers. Furthermore, the active and reactive power outputs of the WTG with PI, FNN and RWPFNN controllers are shown in Figs. 17(c), 18(c) and 19(c). In addition, the active and reactive power outputs of BESS of the PI, FNN and RWPFNN controllers are shown in Figs. 17(d), 18(d) and 19(d). The control commands and signals of the BESS are shown in Figs. 17(e), 18(e) and 19(e). From the experimental results, both the LVRT requirements of the PV system and VRC of the BESS are still fulfilled under the variations of the outputs of the PV and WTG systems. Additionally, the proposed RWPFNN controller possesses fast response with small voltage restoration error comparing with the PI and FNN controllers.

The performance measurings of the PI, FNN and RWPFNN controllers with VRC and active power control of BESS in Case C conditions are compared in Table 4. From Table 4, the IAE, the response time and the MAE of voltage restoration of the proposed RWPFNN controller are significantly lower than both the PI and FNN controllers. Moreover, the IAE, the response time and the MAE of active power control of the proposed RWPFNN controller are still the lowest among three controllers.

V. CONCLUSION

To provide fast response of voltage restoration during grid faults in a microgrid, a VRC based on BESS has been successfully developed in this study. Since the BESS can maintain seamless operation for severe voltage-sag conditions and reduce the impact of intermittent renewable energy, the BESS has been broadly used in the microgrid system nowadays. In this study, two control strategies have been designed to fulfill the voltage restoration of the PCC during grid faults. The first one is the control of PV system to satisfy the requirements of the reactive power support of LVRT according to the grid codes; the second one is the control of BESS to implement the VRC when voltage sags happen. Moreover, the RWPFNN, which combines the merits of the functional advantages of the PN, RFNN and WFNN, has been successfully developed and adopted in the VRC. From the experimental results of the Cimei Island microgrid, it has been verified that the proposed RWPFNN controller can provide fast voltage restoration response which is very helpful to mitigate the transient impact during grid faults of the microgrid.

APPENDIX

To guarantee the convergence of the proposed RWPFNN controller, specific learning-rate factors for the training of the parameters of the RWPFNN can be obtained by using the convergence analysis [38]. First, the error function shown in (19) is considered as a discrete-type Lyapunov function. Then, the variation of the Lyapunov function can be rewritten

as follows:

$$\Delta E(N) = E(N+1) - E(N) \tag{A1}$$

Linearized model of the Lyapunov function is obtained via (21), (25), (28), (31) and (32) as follows [38]:

$$\begin{aligned}
E(N+1) &= E(N) + \Delta E(N) \\
&\cong E(N) + \sum_{lo=1}^{9}\left(\frac{\partial E(N)}{\partial w_{lo}^5}\Delta w_{lo}^5\right) \\
&\quad + \sum_{r=1}^{9}\left(\frac{\partial E(N)}{\partial w_r^4}\Delta w_r^4\right) \\
&\quad + \sum_{k=1}^{9}\sum_{i=1}^{2}\left(\frac{\partial E(N)}{\partial w_{ik}^3}\Delta w_{ik}^3\right) \\
&\quad + \sum_{j=1}^{6}\left(\frac{\partial E(N)}{\partial m_j^2}\Delta m_j^2 + \frac{\partial E(N)}{\partial \sigma_j^2}\Delta \sigma_j^2\right) \\
&= \frac{1}{5}E(N) - \eta_{lo}\sum_{lo=1}^{9}\left(\frac{\partial E(N)}{\partial w_{lo}^5(N)}\right)^2 \\
&\quad + \frac{1}{5}E(N) - \eta_r\sum_{r=1}^{9}\left(\frac{\partial E(N)}{\partial w_r^4(N)}\right)^2 \\
&\quad + \frac{1}{5}E(N) - \eta_{ik}\sum_{k=1}^{9}\sum_{i=1}^{2}\left(\frac{\partial E(N)}{\partial w_{ik}^3(N)}\right)^2 \\
&\quad + \frac{1}{5}E(N) - \eta_m\sum_{j=1}^{6}\left(\frac{\partial E(N)}{\partial m_j^2(N)}\right)^2 \\
&\quad + \frac{1}{5}E(N) - \eta_\sigma\sum_{j=1}^{6}\left(\frac{\partial E(N)}{\partial \sigma_j^2(N)}\right)^2
\end{aligned} \tag{A2}$$

where Δw_{lo}^5, Δw_r^4, Δw_{ik}^3, Δm_j^2, and $\Delta \sigma_j^2$ depict the variations of the connective weights, the means and the standard deviations. If the learning-rate factors of the proposed RWPFNN are designed as:

$$\begin{aligned}
\eta_{lo} &= \frac{E(N)}{5}/\left(\sum_{lo=1}^{9}\left(\frac{\partial E(N)}{\partial w_{lo}^5(N)}\right)^2 + \varepsilon\right), \\
\eta_r &= \frac{E(N)}{5}/\left(\sum_{r=1}^{9}\left(\frac{\partial E(N)}{\partial w_r^4(N)}\right)^2 + \varepsilon\right), \\
\eta_{ik} &= \frac{E(N)}{5}/\left(\sum_{k=1}^{9}\sum_{i=1}^{2}\left(\frac{\partial E(N)}{\partial w_{ik}^3(N)}\right)^2 + \varepsilon\right), \\
\eta_m &= \frac{E(N)}{5}/\left(\sum_{j=1}^{6}\left(\frac{\partial E(N)}{\partial m_j^2(N)}\right)^2 + \varepsilon\right), \\
\eta_\sigma &= \frac{E(N)}{5}/\left(\sum_{j=1}^{6}\left(\frac{\partial E(N)}{\partial \sigma_j^2(N)}\right)^2 + \varepsilon\right)
\end{aligned} \tag{A3}$$

where ε is a small positive constant and (A3) can be reformulated as follows:

$$\begin{aligned}
E(N+1) &\approx \frac{E(N)\varepsilon}{5\left[\sum_{lo=1}^{9}\left(\frac{\partial E(N)}{\partial w_{lo}^5(N)}\right)^2 + \varepsilon\right]} \\
&\quad + \frac{E(N)\varepsilon}{5\left[\sum_{r=1}^{9}\left(\frac{\partial E(N)}{\partial w_r^4(N)}\right)^2 + \varepsilon\right]} \\
&\quad + \frac{E(N)\varepsilon}{5\left[\sum_{k=1}^{9}\sum_{i=1}^{2}\left(\frac{\partial E(N)}{\partial w_{ik}^3(N)}\right)^2 + \varepsilon\right]} \\
&\quad + \frac{E(N)\varepsilon}{5\left[\sum_{j=1}^{6}\left(\frac{\partial E(N)}{\partial m_j^2(N)}\right)^2 + \varepsilon\right]} \\
&\quad + \frac{E(N)\varepsilon}{5\left[\sum_{j=1}^{6}\left(\frac{\partial E(N)}{\partial \sigma_j^2(N)}\right)^2 + \varepsilon\right]} \\
&< \frac{E(N)}{5} + \frac{E(N)}{5} + \frac{E(N)}{5} \\
&\quad + \frac{E(N)}{5} + \frac{E(N)}{5} = E(N)
\end{aligned} \tag{A4}$$

REFERENCES

[1] N. Nasser and M. Fazeli, "Buffered-microgrid structure for future power networks; a seamless microgrid control," *IEEE Trans. Smart Grid*, vol. 12, no. 1, pp. 131–140, Jan. 2021.

[2] A. Hirsch, Y. Parag, and J. Guerrero, "Microgrids: A review of technologies, key drivers, and outstanding issues," *Renew. Sustain. Energy Rev.*, vol. 90, pp. 402–411, Jul. 2018.

[3] J. Liu, J. Li, H. Song, A. Nawaz, and Y. Qu, "Nonlinear secondary voltage control of islanded microgrid via distributed consistency," *IEEE Trans. Energy Convers.*, vol. 14, no. 8, pp. 1–8, Feb. 2020.

[4] C. Li, J. Yang, Y. Xu, Y. Wu, and P. Wei, "Classification of voltage sag disturbance sources using fuzzy comprehensive evaluation method," *CIRED-Open Access Proc. J.*, vol. 2017, no. 1, pp. 544–548, Oct. 2017.

[5] S. M. Mohiuddin and J. Qi, "Droop-free distributed control for AC microgrids with precisely regulated voltage variance and admissible voltage profile guarantees," *IEEE Trans. Smart Grid*, vol. 11, no. 3, pp. 1956–1967, May 2020.

[6] M. Nasiri and R. Mohammadi, "Peak current limitation for grid side inverter by limited active power in PMSG-based wind turbines during different grid faults," *IEEE Trans. Sustain. Energy*, vol. 8, no. 1, pp. 3–12, Jan. 2017.

[7] A. Mojallal and S. Lotfifard, "Enhancement of grid connected PV arrays fault ride through and post fault recovery performance," *IEEE Trans. Smart Grid*, vol. 10, no. 1, pp. 546–555, Jan. 2019.

[8] *Grid Connection Regulations for High and Extra High Voltage, Status: 1*, E.ON Netz GmBH, Apr. 2006.

[9] A. Calle-Prado, S. Alepuz, J. Bordonau, J. Nicolas-Apruzzese, P. Cortés, and J. Rodriguez, "Model predictive current control of grid-connected neutral-point-clamped converters to meet low-voltage ride-through requirements," *IEEE Trans. Ind. Electron.*, vol. 62, no. 3, pp. 1503–1514, Mar. 2015.

[10] Y. Jiang, C. Qin, X. Xing, X. Li, and C. Zhang, "A hybrid passivity-based control strategy for three-level T-type inverter in LVRT operation," *IEEE J. Emerg. Sel. Topics Power Electron.*, vol. 8, no. 4, pp. 4009–4024, Dec. 2020.

[11] S. M. Muyeen, "A combined approach of using an SDBR and a STATCOM to enhance the stability of a wind farm," *IEEE Syst. J.*, vol. 9, no. 3, pp. 922–932, Sep. 2015.

[12] W. G. Lee, T. T. Nguyen, H. J. Yoo, and H.-M. Kim, "Low-voltage ride-through operation of grid-connected microgrid using consensus-based distributed control," *Energies*, vol. 11, no. 11, pp. 2867–2884, Oct. 2018.
[13] X. Shen, H. Wang, D. Zhang, J. Li, R. Wang, and Q. Su, "Distributed finite-time secondary voltage restoration of droop-controlled islanded microgrids," *IEEE Access*, vol. 8, pp. 118183–118191, 2020.
[14] M. Shi, X. Chen, J. Zhou, Y. Chen, J. Wen, and H. He, "PI-consensus based distributed control of AC microgrids," *IEEE Trans. Power Syst.*, vol. 35, no. 3, pp. 2268–2278, May 2020.
[15] F. M. Mahdianpoor, R. A. Hooshmand, and M. Ataei, "A new approach to multifunctional dynamic voltage restorer implementation for emergency control in distribution systems," *IEEE Trans. Power Del.*, vol. 26, no. 2, pp. 882–890, Apr. 2011.
[16] P. T. Ogunboyo, R. Tiako, and I. E. Davidson, "Effectiveness of dynamic voltage restorer for unbalance voltage mitigation and voltage profile improvement in secondary distribution system," *Can. J. Elect. Comput. Eng.*, vol. 41, no. 2, pp. 105–115, Spring 2018.
[17] A. Benali, M. Khiat, T. Allaoui, and M. Denaï, "Power quality improvement and low voltage ride through capability in hybrid wind-PV farms grid-connected using dynamic voltage restorer," *IEEE Access*, vol. 6, pp. 68634–68648, 2018.
[18] T. Kandil and M. A. Ahmed, "Control and operation of dynamic voltage restorer with online regulated DC-link capacitor in microgrid system," *Can. J. Electr. Comput. Eng.*, vol. 43, no. 4, pp. 331–341, 2020.
[19] D. G. A. Krishna, K. Anbalagan, K. K. Prabhakaran, and S. Kumar, "An efficient pseudo-derivative-feedback-based voltage controller for DVR under distorted grid conditions," *IEEE J. Emerg. Sel. Topics Ind. Electron.*, vol. 2, no. 1, pp. 71–81, Jan. 2021.
[20] T. A. Naidu, S. R. Arya, R. Maurya, and S. Padmanaban, "Performance of DVR using optimized PI controller based gradient adaptive variable step LMS control algorithm," *IEEE J. Emerg. Sel. Topics Ind. Electron.*, vol. 2, no. 2, pp. 155–163, Apr. 2021.
[21] H. S. Krishnamoorthy, D. Rana, P. Garg, P. N. Enjeti, and I. J. Pitel, "Wind turbine generator–battery energy storage utility interface converter topology with medium-frequency transformer link," *IEEE Trans. Power Electron.*, vol. 29, no. 8, pp. 4146–4155, Aug. 2014.
[22] S. Prakash and S. Mishra, "VSC control of grid connected PV for maintaining power supply during open-phase condition in distribution network," *IEEE Trans. Ind. Appl.*, vol. 55, no. 6, pp. 6211–6222, Nov. 2019.
[23] J. I. Y. Ota, T. Sato, and H. Akagi, "Enhancement of performance, availability, and flexibility of a battery energy storage system based on a modular multilevel cascaded converter (MMCC-SSBC)," *IEEE Trans. Power Electron.*, vol. 31, no. 4, pp. 2791–2799, Apr. 2016.
[24] D. Ranamuka, K. M. Muttaqi, and D. Sutanto, "Flexible AC power flow control in distribution systems by coordinated control of distributed solar-PV and battery energy storage units," *IEEE Trans. Sustain. Energy*, vol. 11, no. 4, pp. 2054–2062, Oct. 2020.
[25] V. M. Hrishikesan and C. Kumar, "Operation of meshed hybrid microgrid during adverse grid conditions with storage integrated smart transformer," *IEEE Open J. Ind. Electron. Soc.*, vol. 2, pp. 315–325, Apr. 2021.
[26] F. Chishti, S. Murshid, and B. Singh, "PCC voltage quality restoration strategy of an isolated microgrid based on adjustable step adaptive control," *IEEE Trans. Ind. Appl.*, vol. 56, no. 6, pp. 6206–6215, Nov. 2020.
[27] R. Zhang, B. Hredzak, and J. Fletcher, "Dynamic aggregation of energy storage systems into virtual power plants using distributed real-time clustering algorithm," *IEEE Trans. Ind. Electron.*, vol. 68, no. 11, pp. 11002–11013, Nov. 2021.
[28] S.-Y. Chen, Y.-H. Hung, and S.-S. Gong, "Speed control of vane-type air motor servo system using proportional-integral-derivative-based fuzzy neural network," *Int. J. Fuzzy Syst.*, vol. 18, no. 6, pp. 1065–1079, Dec. 2016.
[29] Y. Fang, J. Fei, and T. Wang, "Adaptive backstepping fuzzy neural controller based on fuzzy sliding mode of active power filter," *IEEE Access*, vol. 8, pp. 96027–96035, 2020.
[30] Y. Q. Lv, C. K. M. Lee, Z. Wu, H. K. Chan, and W. H. Ip, "Priority-based distributed manufacturing process modeling via hierarchical timed color Petri net," *IEEE Trans. Ind. Informat.*, vol. 9, no. 4, pp. 1836–1846, Nov. 2013.
[31] Y.-C. Hung, F.-J. Lin, J.-C. Hwang, J.-K. Chang, and K.-C. Ruan, "Wavelet fuzzy neural network with asymmetric membership function controller for electric power steering system via improved differential evolution," *IEEE Trans. Power Electron.*, vol. 30, no. 4, pp. 2350–2362, Apr. 2015.
[32] K.-H. Tan, "Squirrel-cage induction generator system using wavelet Petri fuzzy neural network control for wind power applications," *IEEE Trans. Power Electron.*, vol. 31, no. 7, pp. 5242–5254, Jul. 2016.
[33] F.-J. Lin, I.-F. Sun, K.-J. Yang, and J.-K. Chang, "Recurrent fuzzy neural cerebellar model articulation network fault-tolerant control of six-phase permanent magnet synchronous motor position servo drive," *IEEE Trans. Fuzzy Syst.*, vol. 24, no. 1, pp. 153–167, Feb. 2016.
[34] S. Ganjefar and M. Tofighi, "Single-hidden-layer fuzzy recurrent wavelet neural network: Applications to function approximation and system identification," *Inf. Sci.*, vol. 294, pp. 269–285, Feb. 2015.
[35] C.-C. Yeh, C.-S. Chen, T.-T. Ku, C.-H. Lin, C.-T. Hsu, Y.-R. Chang, and Y.-D. Lee, "Design of special protection system for an offshore island with high-PV penetration," *IEEE Trans. Ind. Appl.*, vol. 53, no. 2, pp. 947–953, Mar. 2017.
[36] T. T. Ku, C. S. Chen, C. T. Hsu, and C. H. Lin, "Enhancement of island microgrid transient stability by battery energy storage system," *Int. J. Ind. Electron. Elect. Eng.*, vol. 7, no. 1, pp. 46–50, Jan. 2019.
[37] F.-J. Lin, C.-I. Chen, G.-D. Xiao, and P.-R. Chen, "Voltage stabilization control for microgrid with asymmetric membership function-based wavelet Petri fuzzy neural network," *IEEE Trans. Smart Grid*, vol. 12, no. 5, pp. 3731–3741, Sep. 2021.
[38] F.-J. Lin, K.-H. Tan, W.-C. Luo, and G.-D. Xiao, "Improved LVRT performance of PV power plant using recurrent wavelet fuzzy neural network control for weak grid conditions," *IEEE Access*, vol. 8, pp. 69346–69358, 2020.
[39] J. Yuan, Y. Lei, L. Wei, C. Tian, B. Chen, and Z. Du, "A novel bridge-type hybrid saturated-core fault current limiter based on permanent magnets," *IEEE Trans. Magn.*, vol. 51, no. 11, pp. 1–4, Nov. 2015.
[40] H. Radmanesh, S. H. Fathi, G. B. Gharehpetian, and A. Heidary, "A novel solid-state fault current-limiting circuit breaker for medium-voltage network applications," *IEEE Trans. Power Del.*, vol. 31, no. 1, pp. 236–244, Feb. 2016.
[41] H. Zhou, J. Yuan, F. Chen, and B. Chen, "Inductive fault current limiters in VSC-HVDC systems: A review," *IEEE Access*, vol. 8, pp. 38185–38197, 2020.

FAA-JENG LIN (Fellow, IEEE) received the B.S. and M.S. degrees in electrical engineering from the National Cheng Kung University, Taiwan, in 1983 and 1985, respectively, and the Ph.D. degree in electrical engineering from the National Tsing Hua University, Taiwan, in 1993. He is currently a Chair Professor with the Department of Electrical Engineering, National Central University, Taiwan. His work has been widely cited. Several of his papers have helped to establish research areas, such as fuzzy neural network control of motor drives and motion control systems, and resonant converters for piezo-ceramic motor drives. His research interests include AC motor drives, power electronics, renewable energies, smart grids, and intelligent and nonlinear control theories. He received the Outstanding Research Awards from the National Science Council, Taiwan, in 2004, 2010, and 2013, and the Outstanding Professor of Engineering Award, in 2016, from the Chinese Institute of Engineers, Taiwan. He is also an IET Fellow. Moreover, he was an Associate Editor of IEEE TRANSACTION ON FUZZY SYSTEMS. He was also the President of Taiwan Smart Grid Industry Association, from 2012 to 2016, and the Chair and a Principal Investigator of the Smart Grid Focus Center, National Energy Project Phase I and II, Taiwan, from 2011 to 2019. He is currently an Associate Editor of IEEE TRANSACTION ON POWER ELECTRONICS and the Executive Director of Taiwan Power Company.

JEN-CHUNG LIAO received the B.S. degree in electrical engineering from Chung Yuan Christian University, Chungli, Taiwan, in 1994, and the M.S. degree in control engineering from the National Chiao Tung University, Hsinchu, Taiwan, in 1996. He is currently pursuing the Ph.D. degree in electrical engineering with the National Central University, Taiwan.

Since 1999, he has been a Senior Researcher with the Chunghwa Telecom Laboratory (TL), Taoyuan, Taiwan. He is currently in-charge of the Project of Energy Management Technology with TL. His research interests include energy-saving technology, power electronics, advanced metering infrastructure (AMI), microgrid, and intelligent control.

CHENG-I CHEN (Member, IEEE) received the Ph.D. degree in electrical engineering from the National Chung Cheng University, Chiayi, Taiwan, in 2009. He is currently an Associate Professor with the Department of Electrical Engineering, National Central University, Taoyuan, Taiwan. His research interests include energy information and communication technology, instrumentation and measurement, and digital signal processing.

PIN-RONG CHEN was born in Hsinchu County, Taiwan, in 1996. She received the B.S. degree in electrical engineering from the National United University, Miaoli, Taiwan, in 2019. She is currently pursuing the M.S. degree with the National Central University, Chungli, Taiwan. Her research interests include intelligent control and microgrid.

YU-MING ZHANG was born in Tainan City, Taiwan, in 1996. He received the B.S. degree in biomechatronic engineering from the National Chiayi University, Chiayi, Taiwan, in 2019. He is currently pursuing the M.S. degree with the National Central University, Chungli, Taiwan. His research interests include intelligent control and microgrid.